molecules

MDPI

Article

Studies of Benzotriazole on and into the Copper Electrodeposited Layer by Cyclic Voltammetry, Time-of-Flight Secondary-Ion Mass Spectrometry, Atomic Force Microscopy, and Surface Enhanced Raman Spectroscopy

Robert Mroczka * and Agnieszka Słodkowska

Laboratory of X-ray Optics, Department of Chemistry, Institute of Biological Sciences, Faculty of Medicine, The John Paul II Catholic University of Lublin, Konstantynów 1J, 20-708 Lublin, Poland; agnieszka.slodkowska@kul.pl
* Correspondence: robert.mroczka@kul.pl; Tel.: +48-81-454-56-39

Abstract: Benzotriazole (BTA) is an important compound that demonstrates the strongest anticorrosion properties of copper and plays a role as a leveler and an additive to the electroplating bath for control of the roughness and corrosion resistance of the electrodeposited copper layer. In this paper, we combined cyclic voltammetry (CV), time-of-flight secondary-ion mass spectrometry (TOF-SIMS), surface enhanced Raman spectroscopy (SERS), and atomic force microscopy (AFM) to study the interaction of BTA with copper surfaces at varied concentrations with and without the presence of chloride ions. We identified the most relevant molecular copper and its complex forms with BTA on the copper electrodeposited layer. BTA is adsorbed and incorporated into the copper surface in monomeric, dimeric, trimeric, tetrameric, and pentameric forms, inhibiting the copper electrodeposition. The addition of chloride ions diminishes the inhibiting properties of BTA. The Cu-BTA-Cl complexes were identified in the forms $C_{12}H_8N_6Cu_2Cl^-$ and $C_6H_4N_3CuCl^-$. Coadsorption of chloride ions and BTA molecules depends on their concentration and applied potential. Chloride ions are replaced by BTA molecules. BTA and chloride ions, depending on their concentration and applied potential, control the copper nucleation processes at the micro- and nanoscales. We compared the abilities and limitations of TOF-SIMS and SERS for studies of the interactions of benzotriazole with copper and chloride ions at the molecular level.

Keywords: copper electrodeposition; benzotriazole; cyclic voltammetry; TOF-SIMS; AFM; SERS

check for updates

Citation: Mroczka, R.; Słodkowska, A. Studies of Benzotriazole on and into the Copper Electrodeposited Layer by Cyclic Voltammetry, Time-of-Flight Secondary-Ion Mass Spectrometry, Atomic Force Microscopy, and Surface Enhanced Raman Spectroscopy. *Molecules* **2023**, *28*, 5912. https://doi.org/10.3390/molecules28155912

Academic Editor: Jia He

Received: 11 July 2023
Revised: 28 July 2023
Accepted: 1 August 2023
Published: 6 August 2023

Copyright: © 2023 by the authors. Licensee MDPI, Basel, Switzerland. This article is an open access article distributed under the terms and conditions of the Creative Commons Attribution (CC BY) license (https://creativecommons.org/licenses/by/4.0/).

1. Introduction

Copper electrodeposition plays an important role in the deposition of copper coatings with varied physicochemical properties that can be controlled by the composition of the electroplating bath, e.g., the applied current densities, the time of the deposition process, etc. [1–6]. Due to this reason, copper electrodeposited layers find numerous applications in nano- and micro-electronics [7], as well as as a decorative and protective layer [8]. To control the nano- and microstructure of the deposited copper layer, functional organic additives such as Cl^- [9–11], MPS/SPS [2,12–16], and PEG [17–19] are used. Benzotriazole is applied as a leveler that promotes deposition of a smooth copper surface by inhibition of copper adatom diffusion and passivation of growing copper islands by effective adsorption of BTA molecules on the copper surface [20–24]. Moreover, BTA is known as the strongest copper corrosion inhibitor that controls unfavorable reactions that can potentially occur on the surface [25,26]. Levelling and brightening abilities of BTA during copper electrodeposition are connected with the number of nitrogen atoms chemically bonded to the copper that increase the number of nucleated copper with reduced size [27–30]. Moreover, N-heterocyclic compounds [31] and their oligomers such as 1,3-bis(1-imidazolyl)propane [32], polyethyleneimine or DTAC [33–35], Benzyl-Containing Quaternary Ammonium Salt [36],

1-(4-Ethoxyphenyl)-5-mercapto-1H-tetrazole [37], and Janus Green B [38] can be used as levelers for acid copper plating. BTA can also form an inhibiting film on the copper electrodeposited layer after immersion in BTA solution [39]. Numerous studies were devoted to the interaction of BTA with oxide-free [26,40–52] and oxide-covered [28,52] copper surfaces. However, the exact mechanism of interaction between BTA and copper surfaces is very often controversial and contradictory [25,53,54]. Generally, it is proposed that BTA can interact with copper in two ways: (1) via the formation of copper metal complexes through nitrogen atoms [25,28,30,47,55,56] that develop polymeric chains [25,26,30,50,52,57–61] or (2) by adsorption in molecular form to the copper surface [43,62–64]. The formation of Cu(I)BTA complex form in neutral and acidic (sulfuric acid) solutions is favored by a higher anodic potential and higher pH, while molecular form is favored by a negative and lower potential [43,57,63–65]. Nevertheless, analysis of the interaction of BTA with copper surfaces with or without the presence of chloride ions under real electrodeposition conditions was carried out only by a few researchers [20–24,66,67]. On the other hand, the latter studies [20,67] were based on only the electrochemical balance technique for determining mass changes during cyclic voltammetry studies. Numerous in situ studies realized via the SERS technique are devoted to solutions consisting of only BTA and sulfuric acid [43,57,63–65]. The limitation of the SERS technique is the strong suppression of the Raman signal for samples prepared in solution consisting of a high concentration of copper sulfate during copper electrodeposition, which determines a noticeable variation in the morphology of the substrate during copper electrodeposition. On the other hand, XPS studies of BTA-copper interactions were carried out for copper immersed in solution containing 50 mM $CuSO_4$ and 10 mM KCl at pH ranging from 4 to 6 [58]. The XRD studies allow for the determination of the molecular Cu(II)BTA [68], Cu(I)BTA [69], and Cu(I)BTACl complexes [70,71] structures. Nevertheless, it is obvious that the molecular interactions of BTA with copper with and without chloride ions under real copper electrodeposition conditions are significantly different. For the determination of the molecular structure and interactions of BTA with the copper surface, a few attempts were carried out using the TOF-SIMS technique [52,72–76]. Moreover, the interaction of similar compounds with copper was examined by TOF-SIMS [35,39]. However, no trials have been devoted to the analysis of the copper electrodeposition under the static regime of TOF-SIMS that allows for the resolution of the molecular structure of Cu-BTA. Instead of that, dynamic modes of TOF-SIMS that allow determination of the distribution of elements incorporated into copper deposits obtained from electroplating baths consisting of BTA were carried out [66,77]. Recently, we showed [15,16,19] that our optimized method that relies on the withdrawal of wire from the electroplating bath during cyclic voltammetry experiments can be successfully applied to the determination of interactions SPS/MPS/Cl/PEG on the copper surface by the TOF-SIMS method.

In this paper, we expand our studies and for the first time combine CV, TOF-SIMS, SERS, and AFM techniques for investigations of BTA interactions with metallic copper and copper ions with and without chloride ions at varied BTA concentrations in the following aspects: (1) the evaluation of the most relevant form of BTA on the copper surface and its reactions with copper and copper ions under open circuit conditions (OCP) and real copper electrodeposition regime; (2) the examination of the complex and molecular formation of Cu-BTA and Cu-BTA-Cl^- on the copper surface under OCP and cyclic voltammetry conditions; (3) the determination of the influence of BTA/Cl^- copper interaction on the morphology of obtained copper layers at nanoscale; (4) the explanation and molecular analysis incorporated of BTA and Cu-BTA complexes into copper deposit postulated previously [21]. In our work, we applied, for the first time, static TOF-SIMS that provides direct identification of molecular forms of BTA/Cu/Cl^- species on the copper surface. The task set in points (1), (2), and (4) allows to formulate, evaluate, and unify the known most relevant interactions between BTA, copper, copper ions, and/or chloride ions postulated during copper electrodeposition [20–24,66,67], which is important for the preparation and optimization of industrial copper electroplating baths containing BTA. Moreover, the

proposed mechanism of interactions between BTA and copper can be useful for a better understanding of known models of copper anticorrosion properties of BTA [28,30,40–52].

2. Results and Discussion

2.1. Dip-Coating (DC) Experiments on the Bare Nitinol Wire and Pre-Plated Nitinol Wire—Evaluation of the Chemistry of Benzotriazole with Copper and Chloride Ions under a Non-Electrochemical Condition

Figure 1 shows the distribution of the most prominent negative and positive fragments identified in the TOF-SIMS spectra for samples 1–20. Samples were prepared by immersing nitinol or nitinol wire covered by a copper layer deposited from the base solution into solutions of varied composition (Table 1). The method of preparation is provided in the section Materials and Methods. The m/z ratios and assignments of selected fragments identified in the TOF-SIMS spectra are included in Table 2.

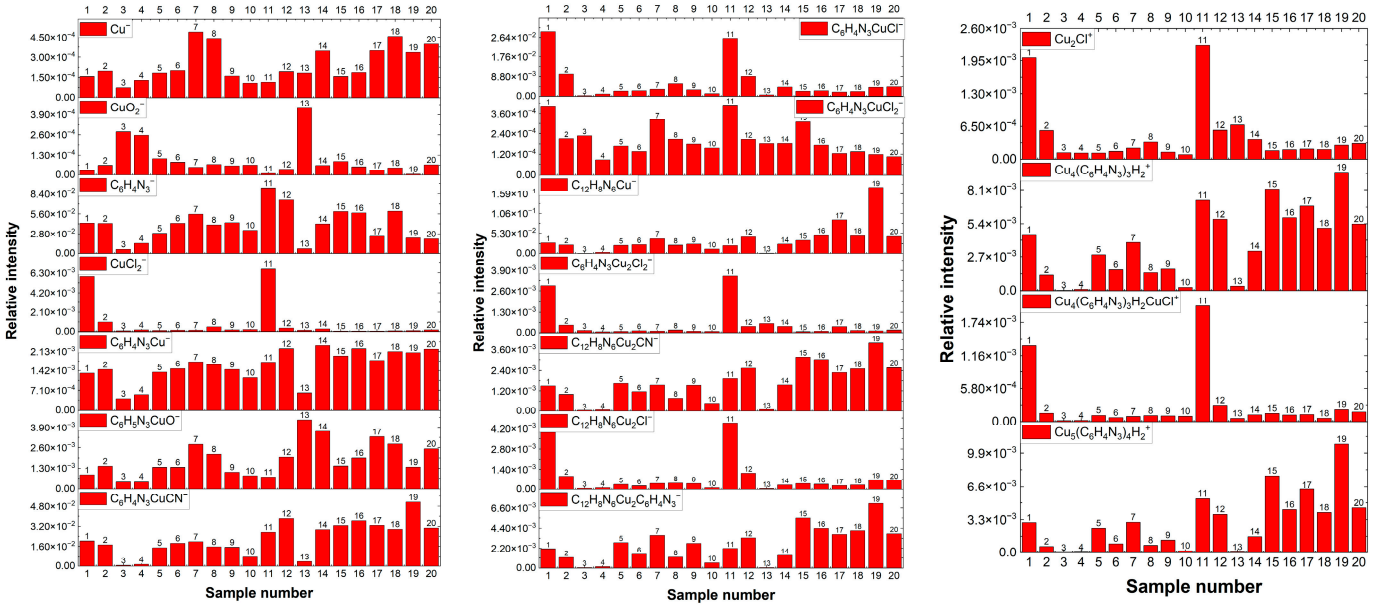


Figure 1. Intensity distribution of selected negative and positive fragments identified in the TOF-SIMS spectra.

Table 1. The assignment of samples that were obtained by the dip-coating experiment. The scheme of assignments: NiTi—nitinol wire immersed for 60 s; NiTi/rinsing—nitinol wire immersed for 60 s and then rinsed; Cu—nitinol wire pre-plated by copper and immersed for 60 s; Cu/rinsing—nitinol wire pre-plated by copper immersed for 60 s and then rinsed.

	NiTi	NiTi/Rinsing	Cu	Cu/Rinsing
0.1M BTA/6.25 mM $CuCl_2$	1	2	11	12
0.1M BTA/6.25mM $CuCl_2$/0.1M H_2SO_4	3	4	13	14
0.1M BTA/0.1M $Cu(NO_3)_2$	5	6	15	16
1.25 mM BTA/0.78mM $CuSO_4$	7	8	17	18
0.39 mM BTA/0.39mM CuCl	9	10	19	20

Table 2. The m/z assignment of negative and positive fragments identified in the TOF-SIMS mass spectra.

No.	Center Mass (u)	Assignment
1	62.99	Cu^-
2	76.07	$C_6H_4^-$
3	90.08	$C_6H_4N^-$
4	94.98	CuO_2^-
5	95.99	SO_4^-
6	97.00	HSO_4^-
7	97.95	$CuCl^-$
8	118.11	$C_6N_3H_4^-$
9	123.96	$CuCNCl^-$
10	132.93	$CuCl_2^-$
11	181.09	$C_6H_4N_3Cu^-$
12	198.11	$C_6N_3H_5CuO^-$
13	207.13	$C_6H_4N_3CuCN^-$
14	216.10	$C_6H_4N_3CuCl^-$
15	251.12	$C_6H_4N_3CuCl_2^-$
16	299.25	$C_{12}N_6H_8Cu^-$
17	314.02	$C_6H_4N_3Cu_2Cl_2^-$
18	388.26	$C_6H_4N_3C_6H_4N_3Cu_2CN^-$
19	397.24	$C_6H_4N_3C_6H_4N_3Cu_2Cl^-$
20	480.40	$C_6H_4N_3C_6H_4N_3C_6H_4N_3Cu_2^-$
21	62.93	Cu^+
22	125.86	Cu_2^+
23	153.86	$Cu_2N_2^+$
24	160.83	Cu_2Cl^+
25	243.92	$Cu_2C_6H_4N_3^+$
26	605.89	$Cu_4(C_6H_4N_3)_3^+$
27	705.80	$Cu_4(C_6H_4N_3)_3H_2CuCl^+$
28	786.87	$Cu_5(C_6H_4N_3)_4^+$

After mixing $CuCl_2$ and BTA (1, 2, 11, and 12 samples), green precipitation was formed, while for solutions consisting of sulfuric acid (samples 3, 4, 13, and 14), the precipitation was not formed. For other solutions, no changes were observed. In the highest mass range, three characteristic positive fragments corresponding to the Cu-BTA adducts were identified. The fragments with mass m/z = 605.89, 703.80, and 786.87 correspond to $Cu_4(BTA)_3^+$, $Cu_4(BTA)_3CuCl^+$, $Cu_5(BTA)_4^+$, and BTA = $C_6H_4N_3$, respectively. The positive fragments assigned as $Cu_4(BTA)_3^+$ and $Cu_5(BTA)_4^+$ were identified previously by TOF-SIMS on the copper surface immersed for 10 min in 0.01 M BTA by Notoya et al. [76]. It showed that in the acidic (pH 1) and alkaline (pH 13) solutions, the fragments $Cu_4(BTA)_3^+$ and $Cu_5(BTA)_4^+$ were not observed. The mass fragments 607.8 and 788.8 with the same assignment as listed in Table 2 were identified by ESI-TOF from the dispersion of copper nanoparticles covered by a BTA layer prepared by the modified Brust-Schiffrin method [78].

The authors carried out structural optimization by means of the DFT method and assumed the existence of cluster $Cu_6(BTA)_4$. The cluster $Cu_6(BTA)_4$ consists of a compact tetrahedral Cu_4 core covered by two BTA-Cu(I)-BTA units. On the other hand, this model is slightly inconsistent with the molecular assignment of $Cu_5(BTA)_4^+$ identified by mass spectrometry. It seems that the latter fragment identified in TOF-SIMS spectra and in ESI-TOF spectra should consist of a central tetrahedral Cu_4 core, one BTA-Cu(I)-BTA ligand connected to Cu_4, and two separated BTAH ligands connected to the central Cu_4, as shown in Figure 2.

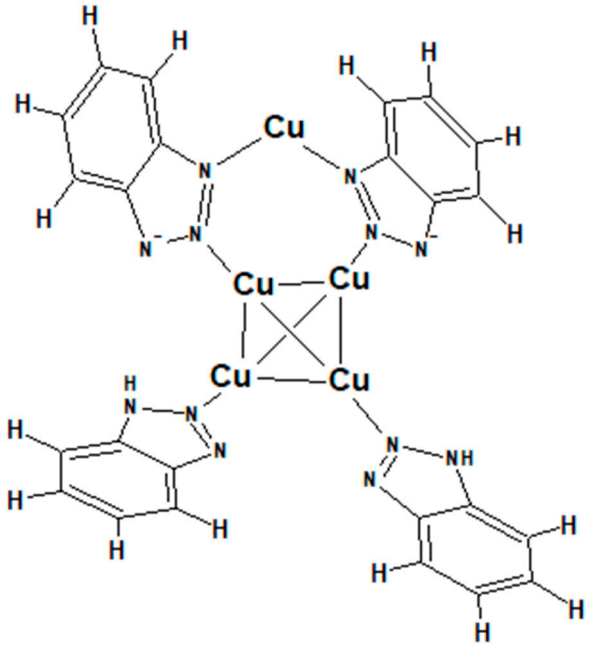


Figure 2. Proposed to simplify the molecular structure of $Cu_5(BTA)_{4^+}$. The optimized molecular structure of $Cu_6(BTA)_4$ can be found elsewhere [61].

Moreover, the slightly higher yield of $Cu_4(BTA)_{3^+}$ than $Cu_5(BTA)_{4^+}$ suggests a second, very stable structure containing three BTA ligands connected to a central, compact Cu_4 core. In this scenario, one BTA ligand forms two N-Cu bonds with core Cu4, while two other BTAH ligands are connected only by one N-Cu bond. The second possible structure of Cu-BTA adducts that explain interactions of BTA with copper assumes the existence of a polymeric linear structure of $[Cu(I)\text{-}BTA\text{-}Cu(I)]_n$. For linear forms, we should expect that the yield of fragments decreases as the mass of fragments increases, which is typical for linear polymers identified in the TOF-SIMS mass spectra [19]. $Cu_4(BTA)_{3^+}$ and $Cu_5(BTA)_{4^+}$ in the mass spectra should be lower than the fragments $Cu_3(BTA)_{2^+}$ and $Cu_2(BTA)^+$. However, the lack of the fragments $Cu_3(BTA)_{2^+}$ and $Cu_2(BTA)^+$ with significantly greater abundance than $Cu_4(BTA)_{3^+}$ and $Cu_5(BTA)_{4^+}$ is determined by the compact, cyclic form of the latter fragments.

Only the fragment $Cu_2(BTA)^+$ with a similar yield was identified, pointing out that BTA can also be bonded to Cu in monodentate form.

The above consideration supports the model of cluster molecular structure proposed in Figure 2 and by Salorinne et al. [78].

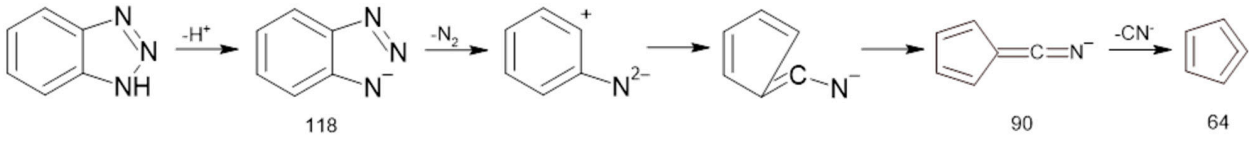
For samples 1 and 11, we identified the fragment $Cu_4(BTA)_3CuCl^+$. After rinsing (samples 2 and 12), the intensity of $Cu_4(BTA)_3CuCl^+$ significantly diminishes for nitinol on the copper substrate. After rinsing, the intensity of $Cu_4(BTA)_3CuClH_{2^+}$ is very low and similar to the samples that do not contain chloride ions (samples 3–10 and 13–20). It means that the Cu-BTA-Cl complex is very soluble in rinsing solution. In acidic solutions (samples 3, 4, 13, and 14), the Cu-BTA-Cl complex and green precipitation were not observed. Furthermore, the lack of fragment $Cu_4(BTA)_3CuCl^+$ for samples 3, 13 and 4, 14 is consistent with this observation. For sample 13, the very low intensity of the fragments $Cu_4(C_6H_4N_3)_{3^+}$ and $Cu_5(BTA)_{4^+}$ indicates that the formation of the polymeric form of Cu(I)-BTA is strongly inhibited in acidic solutions (pH < 1), as previously reported [43,76,79,80]. However, the significantly lower intensity of $Cu_4(BTA)_{3^+}$ for the nitinol substrate (sample 3) in comparison to the copper substrate (sample 13) suggests that the formation of some amount of Cu(I)-BTA polymeric complexes is possible on the copper substrate.

After rinsing, the intensity of the fragment $Cu_4(BTA)_{3^+}$ only slightly increases for nitinol substrate (sample 4), while on copper (sample 14), it strongly rises. It means that metallic copper forms chemical bonds with BTA in acidic solution, similarly to the complex Cu(I)-BTA that is observed for samples 11, 12, and 14–20. This observation is supported

by the similar distribution of the following fragments: $C_6H_4N_3Cu^-$, $C_6H_4N_3CuCN^-$, $C_{12}H_8N_6Cu^-$, $C_{12}H_8N_6Cu_2CN^-$, and $C_{18}H_{12}N_9Cu_2^-$. Furthermore, the chemical bonds of BTA with the nitinol substrate were not identified in the TOF-SIMS spectra.

Identification of the negative high mass fragments: $C_6H_4N_3$- (m/z = 118), $C_6H_4N^-$, $C_{12}H_8N_6Cu^-$ (m/z = 299), $C_{18}H_{12}N_9Cu_2^-$ (m/z = 480), $C_{24}H_{16}N_{12}Cu_3^-$ (m/z = 661), as well as $Cu_4(BTA)_3$ and $Cu_5(BTA)_4$ was reported previously [52,76].

The fragmentation of BTA molecules during bombardment by the Bi primary beam is as follows (1):



(1)

In the first step, the hydrogen cation H^+ is released, yielding the anionic form of BTA (m/z = 118). The free electron pair indicated by the sign minus is highly delocalized on three nitrogen atoms. In the second step, N_2 is subtracted, giving a carbocation that, after intermolecular arrangement, forms a ketenimine anion (m/z = 90). Finally, after releasing the cyanide anion CN^-, the neutral form of 1,2,4-cyclopentatriene is yielded (m/z = 64). The lack of fragments with mass 64 in positive as well as negative modes proves the proposed pathway of fragmentation of BTA. A similar fragmentation pathway was proposed previously [81]. On the other hand, the experimental mass spectra by electron ionization were obtained in the positive ion mode for masses 119, 91, and 64. In more recent results, BTA characteristic fragments in the negative ion mode were identified for m/z = 118 after electron spray ionization [78] and by TOF-SIMS [52,76] that strongly support the fragmentation pathway (1). Moreover, for positive ion mode, the fragment with mass 119 was not observed as it corresponds to the neutral form of BTA. On the other hand, we identified $C_6H_6N_3^+$ as the protonated form of BTA in the positive ion mode.

The anionic fragments of $Cu_x(BTA)_y^-$ are yielded from linear dimeric (BTA-Cu-BTA), trimeric (BTA-Cu-BTA), and tetrameric forms (BTA-Cu-BTA-Cu-BTA-Cu) of Cu-BTA. This hypothesis is based on the intensity ratio of the fragments m/z 299, 480, and 661 that is equal to 662:87:1.7 identified in the TOF-SIMS spectra. Such an intensity distribution is typical for linear forms of polymers, where the intensity of larger mass fragments rapidly decreases. As it was pointed out in the positive mass spectra, we did not notice this kind of fragmentation. In the case of the polymeric form of $[Cu\text{-}(BTA)]_n$ on the copper surface, every BTA subunit involves one nitrogen bond to the copper substrate, while the remaining two nitrogen atoms are connected to two copper adatoms [28,30]. In consequence, two atoms of nitrogen are coordinated to two copper adatoms, while in dimeric form, only one atom of nitrogen is coordinated to one copper adatom. As a result, the less coordinated Cu atoms involved in the Cu-BTA complex structure, the higher the binding energy of every BTA unit [27,30,82].

The most prominent fragment of BTA in deprotonated form ($C_6H_4N_3^-$) was detected in all samples except samples 3 and 13, which contained sulfuric acid. For those samples, the intensity of all negative fragments is significantly reduced, with the exception of the hydroxylated form of BTA, $C_6H_4N_3CuOH^-$, for sample 13. After rinsing, a significant increase in all BTA and Cu-BTA fragments for copper substrate (sample 14) occurs, while for nitinol, that effect is not observed (sample 4). We can conclude that the complex forms of Cu(I)-BTA can be formed on the copper surface in acidic solution.

The distribution of the intensity fragments $CuCl_2^-$, $C_6H_4N_3CuCl^-$, $C_6H_4N_3Cu_2Cl_2^-$, $C_{12}H_8N_6Cu_2Cl^-$, Cu_2Cl^+, and $Cu_4(BTA)_3CuCl^+$ is very similar. High intensity of the latter fragments is observed for samples 1 and 11 from solutions containing green complex and significantly decreases after rinsing (samples 2 and 12). It proves that the negative fragments containing chloride ions are yielded from the same molecular structure as $Cu_4(BTA)_3CuCl^+$.

2.2. Chemistry of Copper Surface after Copper Electrodeposition from Electrolyte Containing BTA without Chloride Ions—Cyclic Voltammetry and TOF-SIMS Measurements

Figure 3 depicts cyclic voltammetry curves for 0, 2, 5, 10, 20, 30, and 50 ppm of BTA in solution containing 0.225 M $CuSO_4$ and 0.56 M H_2SO_4. For the base electrolyte, during reverse scan, a cathodic peak around −0.25 V (V vs. Ag/Ag_2SO_4) occurs (Figure 3). It suggests that copper deposition can be controlled by diffusion. After injection of BTA, the cathodic peak is shifted towards more negative potentials for reverse scanning. The greater the BTA concentration, the greater the shift of potential toward a negative value (Figure 3). On the other hand, for forward scanning, the current density is constantly reduced with increasing BTA concentration. It means that BTA acts as a suppressor and increases overpotential during copper electrodeposition. Similar findings were reported previously [20–22].

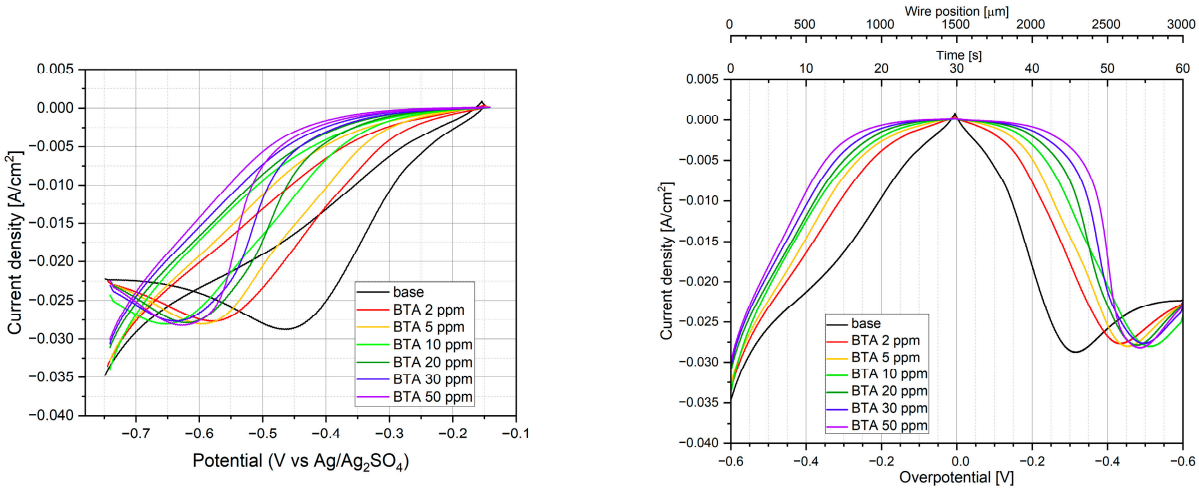


Figure 3. Cyclic voltammetry for base solution and BTA concentrations: 2, 5, 10, 20, 30, and 50 ppm. On the left side, in classical fashion, the right plot shows the wire position, time of electrodeposition, and overpotential. Sweep potential speed: 20 mV/s.

For all CV curves, significant hysteresis is clearly visible. It may be determined by the changes in surface roughness for the forward and reverse scans. When the coordination number of copper atoms on the surface decreases (surface roughness increases), the adsorption energy of BTA increases [28,82]. Surface roughness and morphology of copper surfaces at the nanoscale were examined by atomic force microscopy (see Section 2.11). The occurrence of hysteresis was also observed during copper electrodeposition in the presence of BTA [22] and was explained by different kinds of substrate during forward scan (gold) and reverse scan (copper).

The current density as a function of BTA at wire position 900 µm is shown in Figure 4.

The distribution of current density demonstrates logarithmic behavior according to the formula:

$$j_c = a - b \ln(C_{BTA} + c) \quad (2)$$

where j_c—cathodic current density; C_{BTA}—BTA concentration (ppm); and a, b, c—parameters.

As can be seen in Figure 4, Equation (5) is valid for $C_{BTA} \geq 1$ ppm. In a similar way, we fitted data at wire positions 0.3, 0.6, and 1.2 mm, which corresponded to forward scans. Parameter a decreases as a function of wire position since the applied cathodic potential decreases. For $C_{BTA} \geq 5$ ppm, the parameter c is negligible, and the decrease in C_{BTA} in the bracket of formula (5) is less than 10%. Parameter b is an important factor that plays a role in the correction coefficient for the whole range of applied overpotentials.

Figure 5 depicts the distribution of intensity of the selected fragments: $C_6H_4N^-$, $C_6H_4N_3^-$, $C_6H_4N_3CuOH^-$, $C_{12}H_8N_6Cu^-$, and $C_{18}H_{12}N_9Cu_2^-$ identified in the negative ion mode and $Cu_4(BTA)_{3^+}$, $Cu_5(BTA)_{4^+}$ in the positive mode as a function of wire position

for the base solution and after addition of BTA in the following concentrations: 0, 2, 5, 10, 20, 30, and 50 ppm.

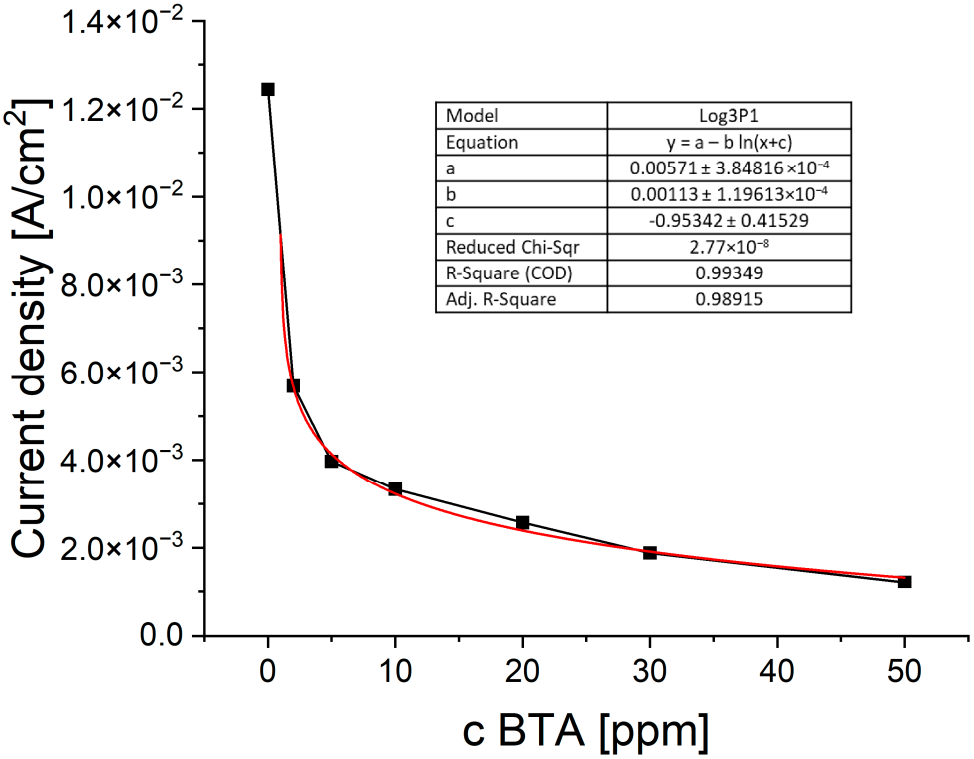


Figure 4. Current density for: 0, 2, 5, 10, 20, 30, and 50 ppm of BTA at wire position 900 µm. It corresponds to the overpotential of −0.25 V for forward scanning (see Figure 3). The red line corresponds to the fitted formula: $j_c = a - b\ \ln(C_{BTA} + c)$, where parameters are: a = 0.0057, b = −0.0011, and c = −0.95.

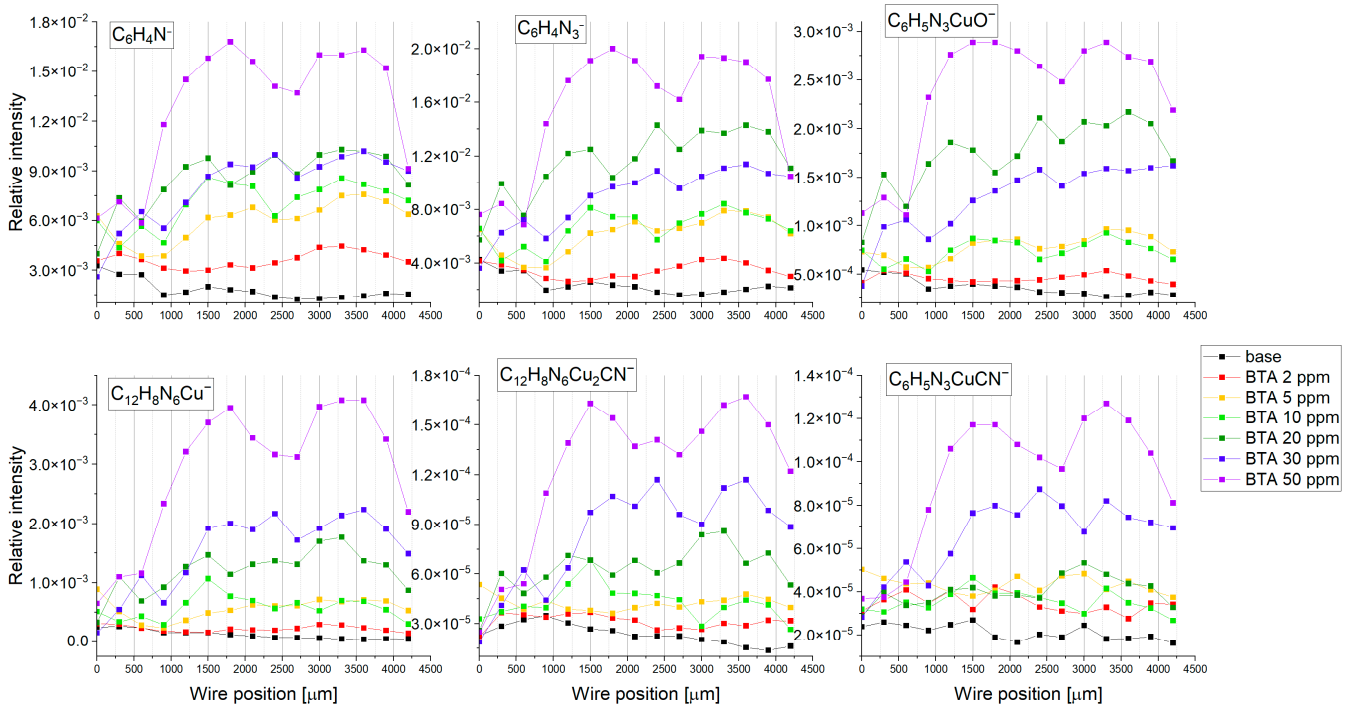


Figure 5. Intensity distribution of the fragments $C_6H_4N^-$, $C_6H_4N_3^-$, $C_6H_4N_3CuOH^-$, $C_{12}H_8N_6Cu^-$, $C_{12}H_8N_9Cu_2CN^-$, and $C_6H_4N_3CuOH^-$ as a function of wire position.

The position of the wire from 0 to 3000 μm corresponds to the applied potential during the cyclic voltammetry experiment. The wire position from 0 to 1500 μm corresponds to the forward scan, while 1500 to 3000 μm corresponds to the reverse scan. The intensity of $C_6H_4N^-$ rises with increasing BTA in solution. Only for 30 ppm of BTA is the intensity of $C_6H_4N^-$ is similar to that for 20 ppm. At 2 ppm of BTA, the intensity is rather stable for the whole CV potential range (wire position 0–3000 μm), with a slight tendency to diminish for lower potentials for forward as well as reverse scan.

The hydroxylated form of BTA assigned to the fragment $C_6H_4N_3CuOH^-$ demonstrates roughly similar distribution to the deprotonated form of BTA, $C_6H_4N_3^-$.

The fragment $C_6H_4N_3CuOH^-$ can be yielded via hydroxylation of the parental BTA molecule and adsorbed via two nitrogen atoms to the copper substrate, while the third nitrogen atom can be attached to the Cu adatom. Under these circumstances, Cu adatom can be hydroxylated during the rinsing of the sample after copper electrodeposition as follows:

$$C_6H_4N_3(ads)\ Cu(ad) + OH^- \rightarrow C_6H_4N_3CuOH^- \quad (3)$$

where $C_6H_4N_3(ads)$ stands for the adsorbed BTA molecule and Cu(ad)—the Cu adatom attached to the BTA.

During sputtering in the TOF-SIMS chamber, the fragment $C_6H_4N_3CuOH^-$ is released from the copper substrate by the cleavage of two Cu-N bonds that attach BTA to the copper substrate. On the other hand, the fragment $C_6H_4N_3CuOH^-$ was also identified for the dip-coated layer of BTA on copper examined in the previous section and by other researchers [52,76] at pH 2 and pH 7. It means that after water evaporation, hydroxylation or oxidation can lead to the same negative ion.

The second important fragment in the negative mode, $C_{12}H_8N_6Cu^-$, corresponds to the dimeric organometallic complex $Cu(BTA)_2^-$. The molecular structure of $Cu(BTA)_2^-$ was studied by the DFT method [25,28,82]. No oxidation or hydroxylated form of $Cu(BTA)_2^-$ was observed. On the other hand, at higher BTA concentrations (20, 30, and 50 ppm), we can expect that BTA exists mostly in dimeric $Cu(BTA)_2^-$, trimeric $Cu_2(BTA)_3^-$, or polymeric forms. The trimeric form $Cu_2(BTA)_3^-$, $C_{18}H_{12}N_9Cu_2^-$, is yielded from the longer, polymeric chain of BTA. No greater polymeric forms, such as the tetrameric or pentameric forms of BTA, were identified in negative mode. Indeed, the fragment $Cu_2(BTA)_3^-$ was identified in the TOF-SIMS spectra at 30 and 50 ppm of BTA.

The lack of the dimeric form $C_6H_4N_3CuOH^-$ in the TOF-SIMS spectra means that the fragment $C_6H_4N_3CuOH^-$ is yielded from single BTA molecules adsorbed on the copper surface (reaction 3) that may coexist with organometallic dimeric forms of BTA.

The contribution of $C_{12}H_8N_6Cu^-$ and $Cu_2(BTA)_3^-$ is low at 2 and 5 ppm of BTA, respectively. Only at 10 ppm for low overpotentials for forward and reverse scan (wire position 1300–1800 μm), the intensity of the organometallic complex $Cu(BTA)_2^-$ significantly grows. On the other hand, the complex $Cu(BTA)_2^-$ covers the surface for the whole overpotential range of 20, 30, and 50 ppm, respectively. Moreover, the polymeric form $Cu_2(BTA)_3^-$ is clearly visible at 30 and 50 ppm. The surface coverage of organometallic complexes in dimeric form $Cu(BTA)_2^-$ as well as in polymeric form $Cu_2(BTA)_3^-$ increases towards more positive potentials, reaching maximum at OCP, while during reverse scan it is rather stable with some tendency to decrease for higher overpotentials (more negative) at 50 ppm (position 2400–3000 μm).

Figure 6 depicts the relationship between intensity and selected fragments as a function of BTA concentration calculated as a mean value of intensity in the cyclic voltammetry region (wire position 0–3000 μm). The standard deviation is related to the deviations of intensity along the wire position (applied potential). The intensity of $C_6H_4N^-$ increases up to 20 ppm. Subsequently, at 30 ppm, the intensity of $C_6H_4N_3^-$ decreases, which may suggest greater coverage of dimeric, trimeric, tetrameric, and pentameric forms of BTA, while at 50 ppm, the intensity of $C_6H_4N_3^-$ rises, reaching its greatest value.

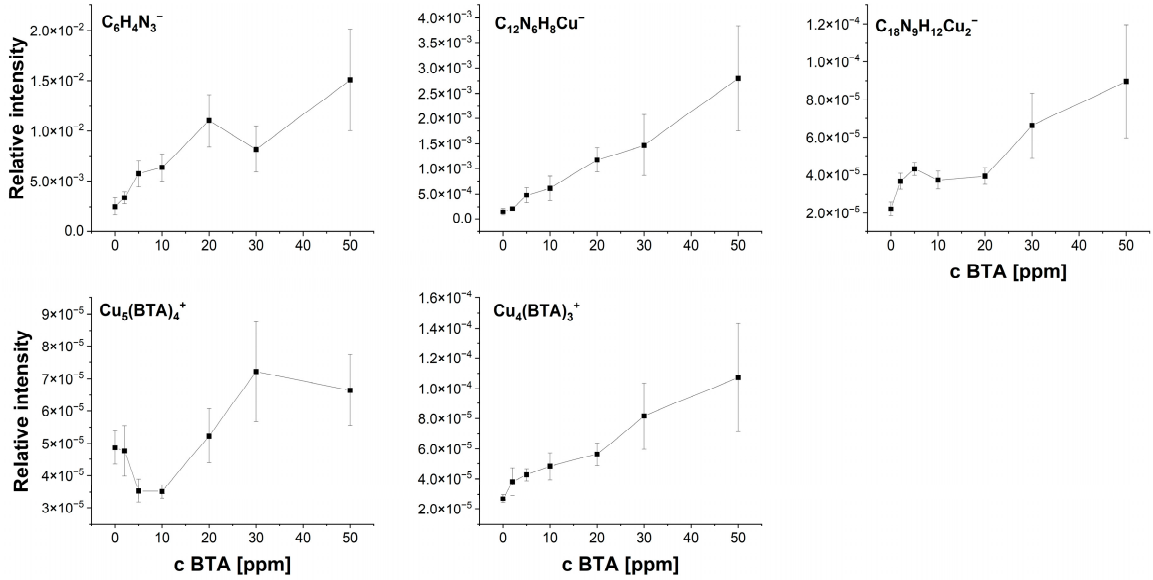


Figure 6. Distribution of intensity of the selected negative fragments: $C_{12}H_8N_6Cu^-$, $C_{18}H_{12}N_9Cu^-$, $C_6H_4N_3^-$, $Cu_4(BTA)_{3^+}$, and $Cu_5(BTA)_{4^+}$ on the copper surface obtained from solutions contained: 0, 2, 5, 10, 20, 30, and 50 ppm of BTA, and 30 ppm of Cl. The standard deviation corresponds to the variation of intensity along the wire position from 0 to 3.0 mm (see Figure 5).

The intensity of the trimeric form $Cu_4(BTA)_{3^+}$ logarithmically grows for BTA concentrations from 2 to 20 ppm, while for 30 and 50 ppm, a greater yield is clearly seen.

It may suggest that for 30 and 50 ppm of BTA, most BTA molecules exist in polymeric forms consisting of three BTA ligands connected to one copper atom. On the other hand, $Cu_5(BTA)_{4^+}$ is observable only at 30 and 50 ppm of BTA. The latter observation may suggest that the molecular arrangement shown in Figure 2 is favorable only at 30 and 50 ppm, while cluster form $Cu_4(BTA)_{3^+}$ is formed for the whole investigated BTA concentration range (2–50 ppm).

The distribution of the anionic trimeric form $Cu_2(BTA)_{3^-}$ fluctuates for 2 to 20 ppm of BTA and significantly increases for 30 and 50 ppm. On the other hand, the intensity for the whole BTA concentration is significantly greater than the value observed for the base solution from some impurities. The most linear intensity distribution occurs for the dimeric form $C_{12}H_8N_6Cu^-$. Only at 50 ppm of BTA is greater intensity observed. However, the linear trend for $C_{12}H_8N_6Cu^-$ may slightly vary depending on applied potential (wire position), as indicated by the standard deviation in Figure 6.

It is widely accepted that the mechanism of inhibiting properties of BTA films on the copper surface is related to the formation of adsorbed molecular species of BTA and Cu(I)BTA complexes. The formation of Cu(I)BTA complexes depends on the pH and potential [43,63,64]. The molecular form of BTA dominates for high-acidity solutions (pH < 1) and for greater (more negative) potentials. The steady-state balance [79] is as follows:

$$Cu^+ + BTAH \leftrightarrow Cu(I)BTA \qquad \rightarrow -0.34\ V \tag{4}$$

$$Cu(I)BTA + e^- \leftrightarrow Cu + BTA\text{-} \qquad -0.15\ V \tag{5}$$

However, our TOF-SIMS results show that organometallic complexes in the form $C_{12}H_6N_8Cu^-$ and polymeric forms $Cu_2(BTA)_{3^-}$ can be formed under our experimental conditions.

The individual forms of BTA monomeric, dimeric, trimeric, tetrameric, and pentameric depend on the BTA concentration and applied potential (Figures 5 and 6) and result from the interaction of metallic copper and Cu^+/Cu^{2+} ions. On the other hand, the influence

of complex Cu(I)BTA and Cu(II)BTA on the exchange current density cannot be directly examined by TOF-SIMS.

Moreover, it was found that Cu^{2+} can form the $Cu(II)(BTA)_4$ complexes at very concentrated solutions of Cu^{2+} (0.1 M) and BTA (0.4 M) at pH 1 [83]. X-ray crystallography studies [68] demonstrated that blue crystals with the formula $Cu(SO_4)(H_2O)(BTAH)_4$ can be formed in this experiment. When the molar ratio BTA:Cu decreases, two BTA ligands can be replaced by water molecules. We reproduced the latter experiment, and we received blue crystals. After immersion of copper wire into the solution over the solid crystal, rapid precipitation of blue crystals was observed. Under our experimental conditions during the CV experiment, we did not observe any precipitation on the copper surface. However, our electrochemical experimental conditions are significantly different, and we cannot rule out the possibility that an invisible thin solid film in the form of $Cu(SO_4)(H_2O)(BTAH)_4$ can be formed on the copper surface.

Moreover, it was also proven [83] that similar complexes can be obtained after immersing copper plates in acidic solution in the presence of SO_4^{2-} ions with the central ion Cu^+. We reproduced that experiment, and we obtained the yellow deposit on the copper plate after several hours. Both blue crystal (Cu(II)BTA) and yellow deposit (Cu(I)BTA) were insoluble in water and diluted sulfuric acid. We carried out TOF-SIMS and SERS measurements for the yellow deposit obtained on the copper plate, and we identified all negative and positive fragments of BTA that existed on the copper wire prepared under the CV experiment. However, our SERS results (Section 2.6) will show that Raman spectra significantly differ for complexes of Cu(I)BTA and SERS data for copper deposited during the CV experiment.

Overall, the existence of the molecular form of BTA in monomeric form $C_6H_4N_3CuOH^-$ and organometallic complexes $C_{12}H_8N_6Cu^-$, $Cu_2(BTA)_{3^-}$, $Cu_4(BTA)_{3^+}$, and $Cu_5(BTA)_{4^+}$ was proven on the copper surface under electrochemical conditions. Molecular adsorption of BTA and complexation of Cu^+ or Cu^{2+} by BTA play a primary role in inhibiting the properties of BTA under copper electrodeposition. For the revision of the TOF-SIMS results, we carried out SERS measurements (Section 2.6).

2.3. Incorporation of BTA into Copper during Copper Electrodeposition from Electrolyte Containing BTA without Chloride Ions—TOF-SIMS Measurements

For a better understanding of the mechanism of copper electrodeposition, we examined the possible incorporation of BTA into copper deposits. The incorporation of benzotriazole was examined by SIMS only in dynamic mode, which does not allow identification of the incorporated molecular form of BTA [66,77]. The copper was electrodeposited for 15 min at a constant current density of -15 mA/cm^2 from a solution of $CuSO_4$ (0.225 M)/H_2SO_4 (0.5 M)/BTA (50 ppm). Subsequently, the copper deposit was immersed in 30% nitric acid for 10 s for etching. Vigorous bubbling was observed on the surface after 3 s. After etching, the copper deposit was rinsed with deionized water and dried in the air.

The intensity ratio $C_{12}H_8N_6Cu^-/Cu_4(BTA)_{3^+}$ is about 10, while $C_{12}H_8N_6Cu^-/C_6H_4N_3CuOH^-$ is about 2.5 (Figure 7). For comparison, the same intensity ratio taken from Figure 2 at wire position 600 μm that corresponds to the current density of -15 mA/cm^2 (see CV curve, Figure 3) equals 16 and 0.8, respectively. It means that BTA is incorporated into deposits mainly in dimeric $C_{12}H_8N_6Cu^-$, trimeric $Cu_4(BTA)_{3^+}$, and tetrameric $Cu_5(BTA)_{4^+}$. The yield of the monomeric form $C_6H_4N_3CuOH^-$ is significantly reduced (16-fold) in comparison to the dimeric form $C_{12}H_8N_6Cu^-$ identified on the copper surface obtained in the CV experiment. Moreover, the contribution of the incorporated $C_{12}H_8N_6Cu^-$ form in comparison to the polymeric form $Cu_4(BTA)_{3^+}$ is also slightly greater.

If we assume that such differences are not determined by different times of electrodeposition (15 min for the etching experiment and 2 min for the CV experiment), we can conclude that incorporation of BTA into the deposit is realized via dimeric forms and polymeric chains. The monomer units are also incorporated, but in a significantly lower amount.

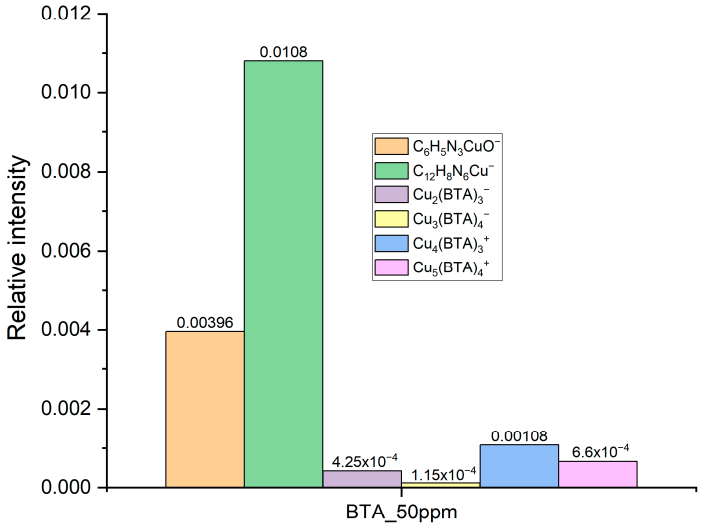


Figure 7. Intensity distribution of $C_6H_4N_3CuOH^-$, $C_{12}H_8N_6Cu^-$, $Cu_2(BTA)_{3^-}$, $Cu_3(BTA)_{4^-}$, $Cu_4(BTA)_{3^+}$, and $Cu_5(BTA)_{4^+}$ on the copper surface after etching in nitric acid.

2.4. Distribution of BTA and Micromorphology of Copper Surface Obtained from Electroplating Bath without Chloride Ions

Figure 8 depicts the distribution of the total ion image and selected BTA fragments: CN^-, $C_6H_4N_{3^-}$, and the backscattered secondary electron image. The darker areas in the total ion image correspond to the low amount of BTA (ions CN^- and $C_6H_4N_{3^-}$).

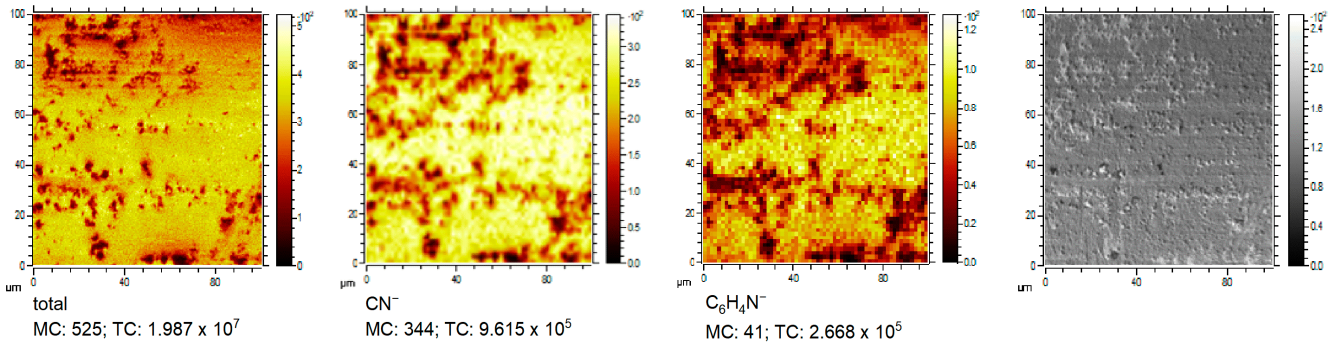


Figure 8. Distribution of selected ions for BTA (50 ppm at wire position 1500 µm). Scanning area: 100 × 100 µm. The right column image shows a backscattered secondary electron image with a resolution of 0.2 µm. The dark areas in the total ion image (left image) correspond to the low amount of BTA as depicted by the CN^- and $C_6H_4N^-$ ions distribution to the crystals visible in the backscattered secondary electron image.

Backscattered secondary electron images (right image) show that crystals are built in areas with very low BTA surface coverage. It directly shows the inhibition properties of BTA in suppressing copper crystal size formation at the microscale. An investigation of the influence of BTA on surface morphology at the nanoscale for all BTA concentrations was examined by AFM (results and discussion in Section 2.11).

2.5. Chemistry of Copper Surface after Copper Electrodeposition from Electrolyte Containing BTA without Chloride Ions—SERS Measurements

Surface Enhanced Raman Spectroscopy (SERS) measurements were carried out for the same sample areas as those conducted for TOF-SIMS. According to our best knowledge, combined studies of TOF-SIMS and SERS for copper electrodeposited layers have never been performed. SERS measurements were conducted with 5 µm steps on the wire area of 40 × 3500 µm that contains 6300 measurement points. Good-quality SERS spectra

containing characteristic bands for BTA were obtained only for samples electrodeposited from solutions consisting of 20, 30, and 50 ppm of BTA.

The distribution of band 795 cm^{-1} in Figure 9 is raw without any postprocessing (smoothing and normalization). It is clearly seen that some spectra recorded at 1500, 1800, and 2200 µm demonstrate greater enhancement than at the other wire position. It is well known that the SERS signal strongly depends on the surface roughness [84,85]. The latter fact determines the significant fluctuation of the Raman signal. The intensity distribution of the band 800 cm^{-1} for BTA 30 ppm is shown in Figure 9.

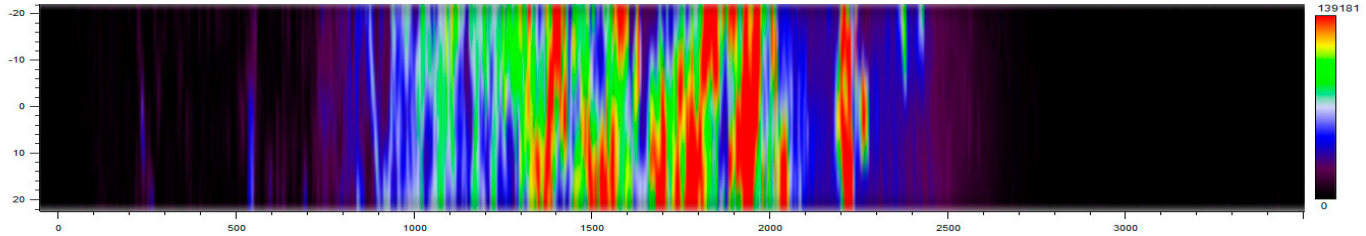


Figure 9. Distribution of intensity in the band 795 cm^{-1} for BTA 30 ppm. The wire position from 0 to 1500 µm corresponds to the forward scan, and the position from 1500 to 3000 µm corresponds to the reverse scan. The position from 3000 to 3500 µm is related to the wire area after switching off current and corresponds to the open circuit potential (OCP).

The distribution of Raman intensity is not uniform. A significant Raman intensity enhancement around wire position 1800 µm can be observed. On the other hand, the Raman signal diminishes for reverse scans at or wire positions greater than 1800 µm. To receive the average value of Raman intensity for a selected area of wire, the whole sample area was divided into a smaller area of 150 × 80 µm that contains 270 measured points. Subsequently, the average Raman intensity from all 270 measurement points was calculated for selected peaks. The distribution of average Raman intensity for bands 795 cm^{-1} and 1395 cm^{-1} for 30 ppm of BTA is shown in Figure 10.

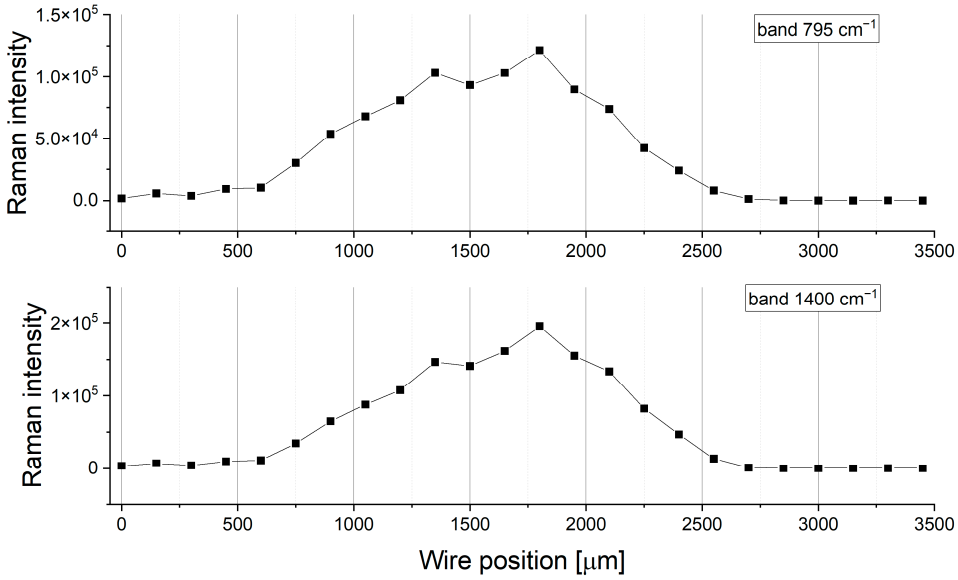


Figure 10. Distribution of Raman intensity bands 795 and 1400 cm^{-1} for 30 ppm of BTA.

The adjacent points are separated by 150 µm and correspond to the applied potential with an interval of 60 mV. In this manner, wire position 0 corresponds to the overpotential −0.6 V, position 1000 µm to the overpotential −180 mV for forward scan, 1500 µm to OCP, etc., similarly as it was carried out for TOF-SIMS measurements.

The BTA molecules (bands 793 cm^{-1}, 1395 cm^{-1}, 1151 cm^{-1}, and 1209 cm^{-1}) are detected at wire position 750 µm, which corresponds to an overpotential −300 mV. At wire

positions from 0 to 750 μm, for overpotentials more negative than −300 mV, the Raman spectra did not contain peaks. When the potential is swept in an anodic direction, the Raman intensity for bands 795 cm^{-1} and 1400 cm^{-1} constantly grows up to −60 mV (wire position 1350 μm). Subsequently, it is stabilized around OCP and again grows up to wire position 1800 μm (overpotential −120 mV, reverse scan). For greater overpotentials, the wire positions continuously decrease up to 2550 μm. At wire positions from 2700 to 3500 μm, no Raman signal was observed. It means that for high overpotentials, more negative than −420 mV BTA molecules are not observed by SERS. Moreover, after switching off current (wire position 3150–3500 μm) under OCP conditions, a Raman signal is also not observed. Contrary to the TOF-SIMS data, at wire positions from 3000 to 4200 μm, BTA molecules were observed with intensity similar to the CV experiment range (wire positions 0–3000 μm).

On the other hand, the CV curves for BTA at 30 ppm (Figure 3) and TOF-SIMS data suggest that BTA surface coverage is still high for greater overpotentials and under OCP after switching off current. It means that the Raman signal is sensitive to the BTA molecules deposited under electrochemical conditions, while under OCP conditions, BTA molecules are not detected, contrary to the TOF-SIMS.

Raman signals can also be significantly diminished for thicker layers of BTA due to the masking of SERS signals from the interface BTA/copper substrate by higher layers of BTA within a multilayer.

For additional insight into this phenomenon, we evaluated SERS data for BTA at 20 ppm and 50 ppm (Figure S1, Supplementary Materials). For 50 ppm of BTA, the Raman signal is strongly enhanced at the wire position from 0 to 600 μm. Subsequently, from 750 to 1800 μm, it is significantly reduced.

It indicates that the SERS signal is limited to the sub- and monolayers of BTA. Consecutively, when BTA layer thickness is reduced at a wire position of 1950 μm, the Raman signal is enhanced due to better access to the copper substrate.

Selected SERS spectra for 30 ppm of BTA at positions of wire: 950, 1100, 1500, 1800, 2100, and 2200 μm at 30 ppm of BTA are shown in Figure 11. For comparison, normal Raman spectra for solid BTA and at 30 ppm of BTA is indicated.

The assignments of selected peaks are included in Table 3.

Table 3. Raman shift and assignment for the most prominent bands identified in the Raman and SERS spectra shown in Figure 11.

Solid BTA	Cu(Poly) [63]	Roughened Cu(Poly) [63]	Chan and Weaver [64]	Band Assignments
429	435	436	440	Skeletal torsion
537	549	553	555	Triazole ring bend
628	630	635	653	Triazole ring torsion
779	785	788	790	Benzene ring breathing
	982	974		SO_4 symmetric stretch
1006	1019		1010	Benzene skeletal and (CH) bend
1022	1025	1024	1020	Benzene skeletal and (CH) bend
1072				(NH) bend
1127	1128	1127		(CH) bend
1147	1134	1145	1140	(NH) bend
1171	1164	1159	1160	Triazole asymmetric stretch and (NH) bend
1206	1193	1196	1190	Triazole-ring breathing mode (C–C–C in-plane bending)
1280	1286	1284	1286	Skeletal stretch (NH) bend and (CH) bend
1374	1377	1380	1370	Fermi resonance with 1385
1387	1388	1391	1385	Combination breathing
	1444		1440	Skeletal stretch

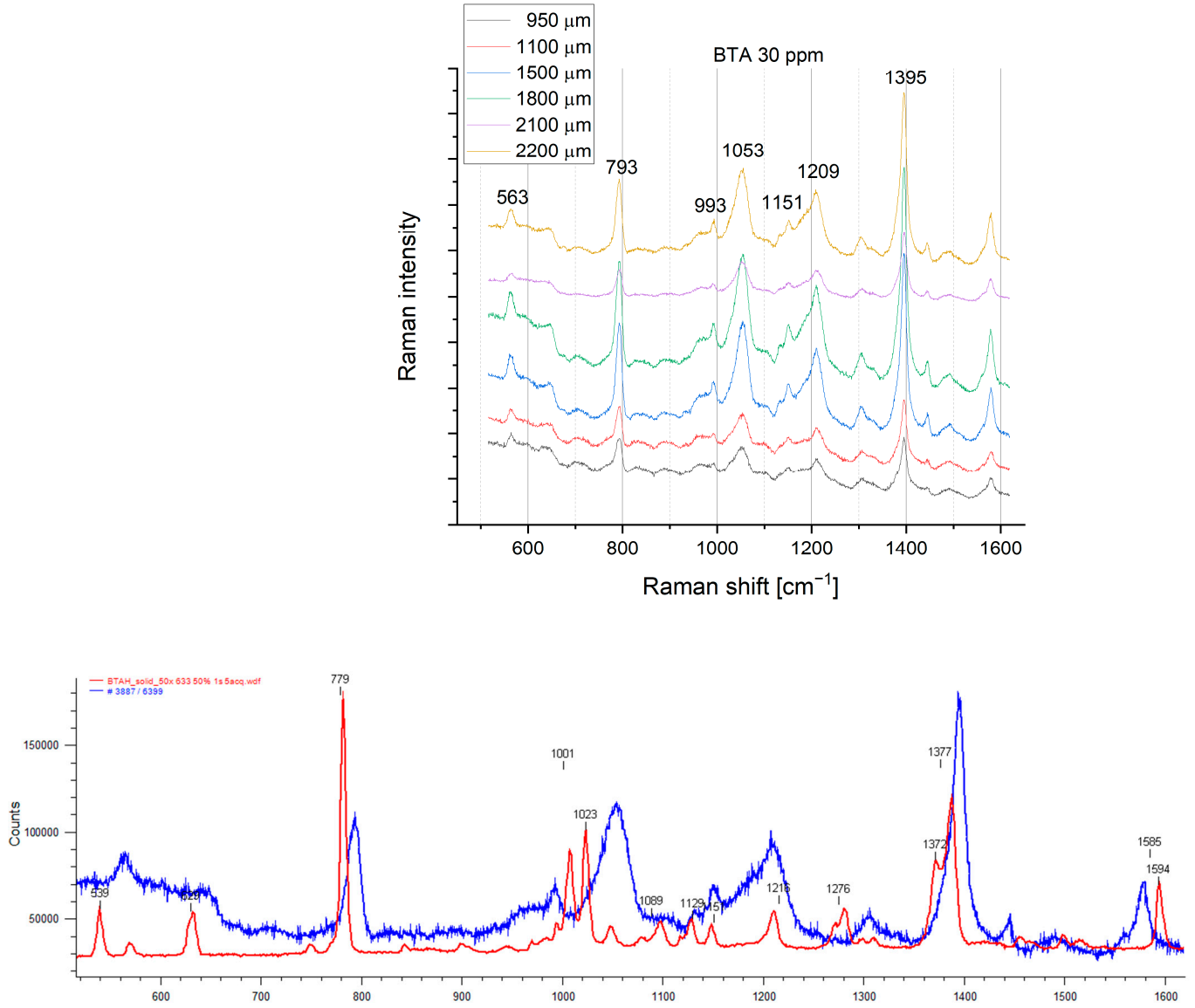


Figure 11. Raman spectra for 30 ppm of BTA at different wire positions (**top graph**) and comparison of Raman spectra for 30 ppm of BTA (blue line) and normal Raman spectra for solid BTAH (red line) (**bottom graph**).

SERS spectra and normal Raman spectra for BTA demonstrate many similarities, while some differences can be easily noticed (Figure 11). The most prominent band at 782 cm^{-1} for normal Raman for BTAH is blueshifted to 794 cm^{-1} for SERS with reduced intensity.

The lack of Raman shift in bands 793 cm^{-1} and 1395 cm^{-1} for different wire positions (different applied potential) means that the benzene ring does not interact directly with the copper substrate. It indicates that the BTA molecules are oriented perpendicular to the copper surface. This observation is consistent with previous studies of BTA adsorption on the copper surface in an acidic environment [64]. However, there were no SERS studies of BTA molecular orientation during copper electrodeposition under real electrochemical conditions.

On the contrary, the second prominent band (1394 cm^{-1}) is only slightly shifted, and intensity significantly increases. The band at 1599 cm^{-1} is redshifted to 1579 cm^{-1}. The main structural affection is observed within 1000–1300 cm^{-1}. The band 1008 cm^{-1} is redshifted to 990 cm^{-1}. The band 1023 cm^{-1} is strongly blueshifted and broadened to 1054 cm^{-1}. The latter phenomenon was not observed by Chant and Weaver [64] for in

situ measurements of BTAH on copper at pH 2, while after emerging into air, the band 1020 cm^{-1} was blueshifted to 1035 cm^{-1} due to possible oxidation of Cu.

$$4Cu + 4BTAH(ads) + O_2 \rightarrow 4\,Cu(I)BTA + 2H_2O \quad (6)$$

A similar blueshift of band 1020 cm^{-1} to 1035 cm^{-1} is observed for the $Cu(II)(BTA)_4$ blue complex (Figure S2, Supplementary Materials). Considering the above, we can safely assume that a broadened band at 1051 cm^{-1} can arise from the oxidation of metallic copper to Cu^{2+} or Cu^{+}. However, the lack of a strong band at 1130 cm^{-1} in SERS spectra that is observed for blue crystal complexes indicates that BTA complexes on the copper surface demonstrate different molecular structures.

Furthermore, the bands 1047 cm^{-1} and 1097 cm^{-1} disappeared, while a significant envelope for the Raman shift from 1150 cm^{-1} to 1210 cm^{-1} is clearly seen. Moreover, the bands 1150 cm^{-1} and 1208 cm^{-1} are still present. The latter band, at 1208 cm^{-1}, possesses the shoulder around 1190 cm^{-1}. It was found [64] that the disappearance of 1095, 1128, and 1208 cm^{-1} bands is SERS and occurs at pH 2. The latter group of peaks is transformed into an intense broad "envelope" containing partially resolved bands at 1140, 1160, and 1190 cm^{-1} with the assignment shown in Table 3 for Cu(poly). On the other hand, it was observed [64] that in a very acidic environment (pH 0) at electrode potential −0.7 V (SCE), the peak at 1190 cm^{-1} disappeared and two distinct bands at 1150 cm^{-1} and 1125 cm^{-1} instead of 1140, 1160, and 1190 cm^{-1} were noticed. At pH 2, after emerging to air, significant dominance of the band 1190 cm^{-1} over 1140 and 1160 and the blueshift 1020 to 1035 cm^{-1} were considered proof of copper oxidation and spontaneous Cu(I)BTA film formation. The band 1190 cm^{-1} was previously [43,62–64] assigned as a Cu(I)BTA complex that is formed at a broad pH and potential range. At pH 0, the band 1190 cm^{-1} [43] constantly rises for potentials more positive than −0.3 V. On the other hand, Honesty et al. [63] calculated the ratio 1190/1140 to estimate the contribution of the Cu(I)BTA complex and molecular form of BTA film to the copper in 0.1 M sulfuric acid. It was concluded that a complex film is formed for a higher positive potential than −0.3 V (vs. Ag/AgCl) for BTA film on roughened polycrystalline copper.

Overall, in our SERS data (Figures 10 and 11), bands 1210 cm^{-1} and 1150 cm^{-1} are clearly seen, while the band around 1190 cm^{-1} is not observed. On the other hand, the significant shoulder at band 1210 cm^{-1} and the broadened strong band at 1051 cm^{-1} indicate the oxidation state of copper and the existence of Cu(I)BTA or Cu(II)BTA complexes. A simultaneously significant amount of BTA in molecular form coexists on the copper surface.

Taking into account the combined CV, TOF-SIMS, and SERS data, we can propose the following mechanism of interaction of BTA with copper during copper electrodeposition (Figure 12).

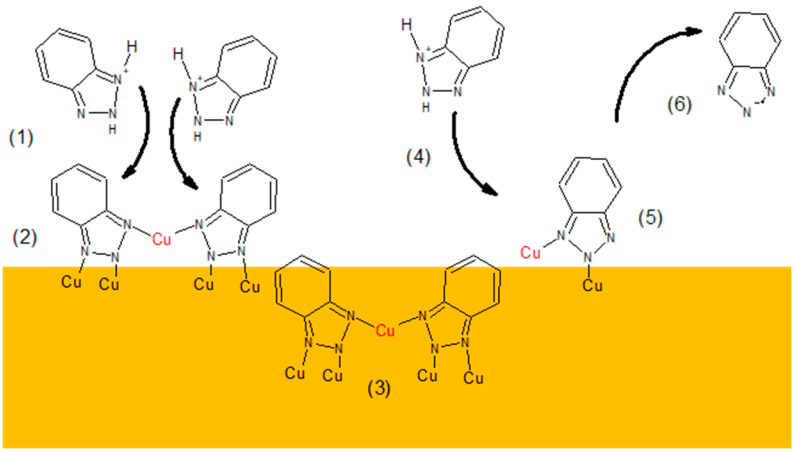


Figure 12. Proposed the cycle of BTA under the copper electrodeposition regime. The red color Cu stands for adatom. The orange color symbolizes the Cu layer. Notice description of brackets in the text.

In the first step, the protonated form of $BTAH_{2^+}$ (1) dissociatively adsorbs on the copper substrate in its molecular form.

$$BTAH_{2^+} \rightarrow BTA^{\bullet} + H^+ + H^{+\bullet} \quad (7)$$

$$BTA^{\bullet} + Cu(ad) \rightarrow Cu\ (BTA) \quad (8)$$

Due to the polycrystalline copper substrate, $BTAH_{2^+}$ molecules can fast adsorb on the substrate in monomeric, dimeric, trimeric, tetrameric, and pentameric forms, depending on the BTA concentration in solution.

The complex in dimeric form, $C_{12}H_8N_6Cu^-$, identified by TOF-SIMS is proceeding in solution as follows:

$$2\ BTAH_{2^+} + Cu+ \rightarrow (BTA\text{-}Cu\text{-}BTA) + 4H^+ \quad (9)$$

However, under acidic conditions, after dissociative adsorption, two $BTA^{\bullet}$ radical ions can catch Cu^+ or Cu_{2^+} ions, as shown in Figure 12.

$$2\ BTA^{\bullet} + Cu^+ \rightarrow BTA\text{-}Cu\text{-}BTA \quad (10)$$

For simplicity, in Figure 12, only the most stable dimeric form is shown (2). The dimeric form is bonded to the copper substrate via four Cu-N bonds. Moreover, copper adatom (red color) links two remaining nitrogen atoms. Copper adatoms may be taken from solution in the form of Cu^+ or Cu^{2+} by BTA molecules to enhance the total binding energy [70]. Results provided in Section 2.2 (incorporation) show that dimeric form is more stable than polymeric form since incorporation of dimeric into copper deposits dominates over polymeric form. On the contrary, on the copper surface, the contribution of polymeric form is slightly greater than that of deposit. The greater binding energy for dimeric rather than polymeric forms was received by Chen et al. [86], while Pejhlan et al. [87] obtained the reverse results.

At 50 ppm, benzotriazole is incorporated into the deposit mostly in the dimeric, trimeric, and tetrameric forms. Only the incorporated dimeric form, which is the most dominant, is shown (3). The monomeric form is also incorporated, though in a significantly lower amount than the other forms. It is due to the lower number of nitrogen atoms involved in bonding a single BTA molecule than longer chains of BTA that desorption is favored in comparison to the dimeric and longer forms. After dissociative adsorption (4) and (5) in the (6) step, the radical form of the BTA species is desorbed. The radical form of BTA can attach hydrogen ions and is released into solution in the protonated form. Consecutively, the protonated form of BTA can undergo pathways (1)–(3) or (4)–(6).

2.6. Copper Electrodeposition from Electrolytes Containing BTA with Chloride Ions—Cyclic Voltammetry Studies

Chloride ions are widely used in copper electrodeposition processes as carriers for other additives such as PEG and SPS [13,16,88]. Moreover, in contrast to BTA, Cl ions initiate copper corrosion. Due to this reason, in this paragraph, we evaluated the interaction of BTA and Cl under electrodeposition conditions.

Figure 13 shows CV curves for base electrolytes (0.225 M $CuSO_4$ and 0.56 M H_2SO_4) after addition of 30 ppm Cl and BTA concentrations 2, 5, 10, 20, 30, and 50 ppm in a classical way (left graph) and as a function of wire position (right graph).

The latter plot will be helpful in a direct comparison of the current density at the selected wire position with the relative intensity (surface coverage) of individual components characteristic of BTA and Cl.

It is clearly visible that after the addition of chloride ions, current density increases since Cl^- acts as an accelerator [9–11]. For a forward scan, the cathodic current peak increases and is shifted to a more positive value. Similar behavior was observed recently [20]. Acceleration behavior is determined by the fact that faster reduction of Cu^{2+} to CuCl forms

in insoluble form on the copper surface than reduction of Cu^{2+} to Cu^{+} without the presence of Cl^{-} [89].

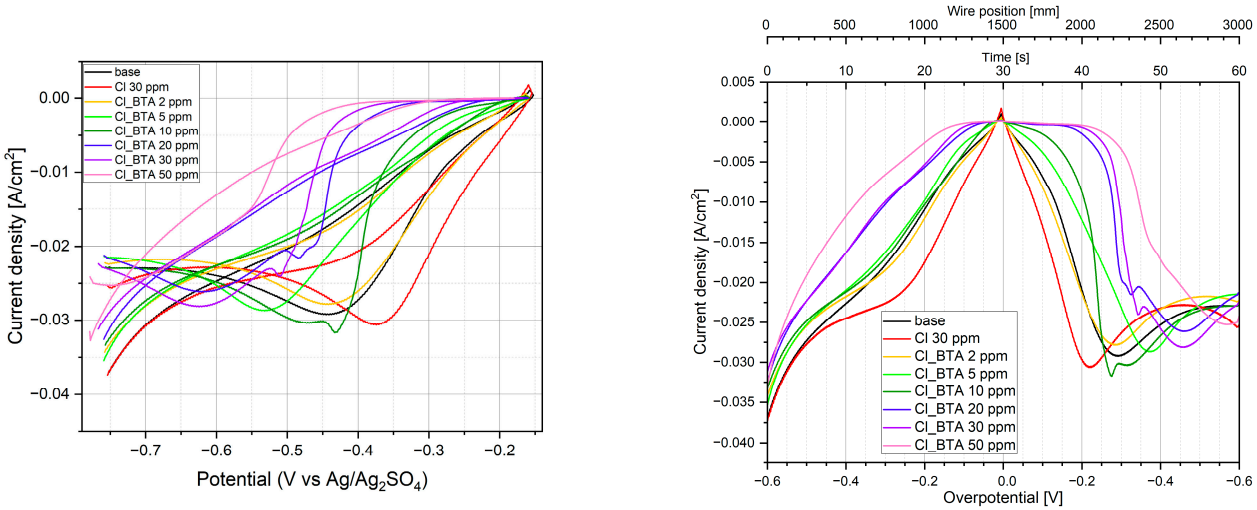


Figure 13. Cyclic voltammetry for base solution and BTA concentrations: 2, 5, 10, 20, 30, and 50 ppm in the presence of chloride ions (30 ppm). The left image demonstrates CV curves in a classical manner; the right plot shows the wire position, time of electrodeposition, and overpotential. Sweep potential speed: 20 mV/s.

After the addition of BTA, CV curves are gradually shifted to lower current densities. For reverse scanning, the cathodic current peak is shifted towards a more negative value that demonstrates the inhibiting properties of BTA. The accelerating abilities of Cl^{-} are gradually reduced. After the addition of 2 ppm of BTA, the accelerating effect of Cl^{-} is completely cancelled, and the CV curve is very similar to that observed for the base solution. A greater amount of BTA enhances the inhibiting properties of BTA. It is interesting that at 10 ppm of BTA, the cathodic peak is greater than for the base solution. Similar behavior was observed elsewhere [20] for BTA (12 ppm) and Cl (10 ppm), a lower $CuSO_4$ amount (0.1 M), and a greater concentration of H_2SO_4 (1.4 M). In our case, at 10 ppm of BTA, greater inhibition properties for reverse scanning are observed for lower overpotentials (more positive than −0.2 V), while the cathodic peak is greater and shifted towards lower overpotentials. It may suggest that some instability or a lower amount of the BTA-Cu-Cl complex can be formed. Indeed, TOF-SIMS data (Section 2.7) shows that the $C_6H_4N_3CuCl^{-}$ fragment demonstrates lower intensity for 10 ppm of BTA than for 5 ppm. The CV curve demonstrates significant hysteresis, similar to what was reported previously [20]. During the reverse scan, the inhibiting properties of BTA substantially increase in comparison to the forward scan. In our electroplating condition, it is very likely determined by different surface roughness during forward and reverse scans that stimulate the strength of BTA adsorption. In the previous studies [20], it was explained by the fact that the substrate was different (gold) during the forward scan than the reverse scan (copper).

When the coordination number of copper atoms on the substrate decreases, the adsorption energy of BTA increases [28,87]. Morphology at the nanoscale was examined by atomic force microscopy (see Section 2.11).

As it is clearly seen in Figure 14, the mean current density fluctuates as a function of BTA concentration. At 2 and 5 ppm of BTA, inhibiting properties of BTA occur. At 10 ppm of BTA, the mean current slightly increases, while at 20 and 30 ppm, it decreases, demonstrating similar values. On the other hand, careful inspection of the CV curve (Figure 13, left plot) shows that inhibiting properties are greater for 30 ppm of BTA than 20 ppm for the whole forward scan and for the reverse scan for potentials more positive than −0.45 V (V vs. Ag/Ag_2SO_4). At the highest BTA concentration (50 ppm), inhibiting properties are the strongest. Such behavior may be determined by possible Cu-BTA-Cl complex formation that moderates the inhibiting abilities of BTA in comparison to the

molecular and complex forms of BTA identified for BTA without chloride ions. The molecular structure of BTA species in the presence of chloride ions on the copper surface was examined by TOF-SIMS (Section 2.7), SERS (Section 2.10), and AFM (Section 2.11).

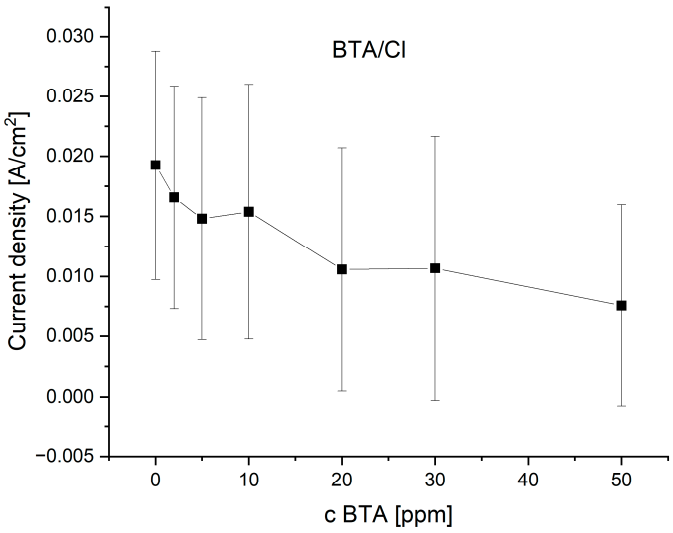


Figure 14. Mean current density as a function of BTA concentration in the presence of chloride ions (30 ppm). Standard deviation stands for current density deviation during the CV experiment for the potential range from −0.6 V to OCP (see Figure 13).

2.7. Chemistry of Copper Surface Deposited from Electrolytes Containing BTA with Chloride Ions—TOF-SIMS Studies

Figure 15 depicts the intensity distribution of selected negative fragments as a function of wire position (applied potential) for the base electrolyte after addition of 30 ppm Cl and BTA at concentrations 2, 5, 10, 20, 30, and 50 ppm.

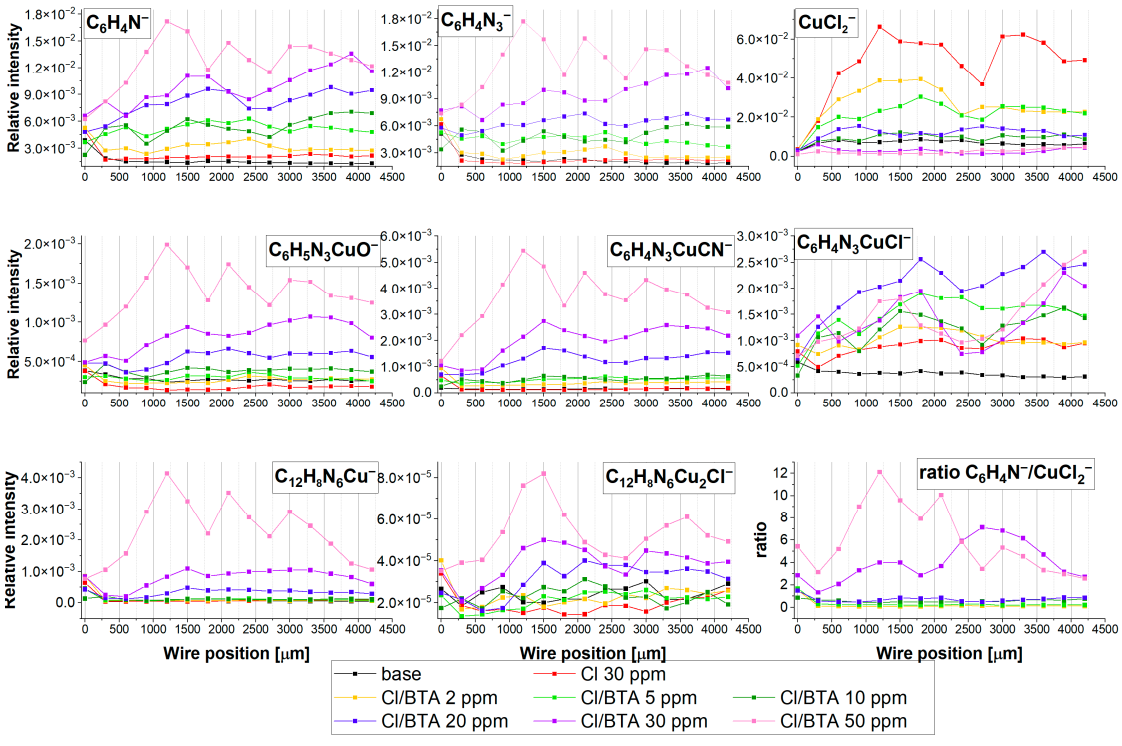


Figure 15. Intensity distribution of the fragments $C_6H_4N^-$, $C_6H_4N_{3^-}$, $C_6H_4N_3CuOH^-$, $C_{12}H_8N_6Cu^-$, $C_{12}H_8N_9Cu_2CN^-$, and $C_6H_4N_3CuOH^-$ and the intensity ratio $C_6H_4N^-/CuCl_{2^-}$ as a function of wire position.

The fragment $CuCl_2^-$ stands for chloride ions directly adsorbed on the copper surface. It is clearly seen that its relative intensity decreases as a function of BTA concentration, meaning chloride ions are partially replaced by BTA molecules. The most rapid replacement is observed at 2, 5, and 10 ppm of BTA. Subsequently, increases in $CuCl_2^-$ intensity at 20 ppm of BTA are observed, while at 30 and 50 ppm of BTA, chloride surface coverage is very low, below intensity for the base electrolyte. It may suggest that at 20 ppm of BTA, the greater intensity of $CuCl_2^-$ may be determined by an additional contribution from other chloride compounds such as $C_6H_4N_3CuCl$ or $C_{12}H_8N_6Cu_2Cl^-$. In this scenario, for 30 and 50 ppm of BTA, chloride ions are not bonded directly to the copper surface since the copper is completely covered by BTA molecules. The small abundance of $CuCl_2^-$ in the base electrolyte is determined by the adsorption of chloride impurities during the transfer of the sample to the TOF-SIMS instrument. That phenomenon was observed and discussed in detail previously [15,16].

BTA molecules are identified in the following forms: $C_{12}H_8N_6Cu^-$, $C_6H_4N_3CuCl^-$, $C_{12}H_8N_6Cu_2Cl^-$, $C_6H_4N_3^-$, and $C_6H_4N_3CuOH^-$. Moreover, additional characteristic fragments for BTA were identified (Figure 15). The intensity of $C_6H_4N_3^-$ rises at 2 and 5 ppm. Subsequently, at 10 ppm, its amount is comparable to 5 ppm, while for greater BTA concentrations, it linearly grows (Figure 16).

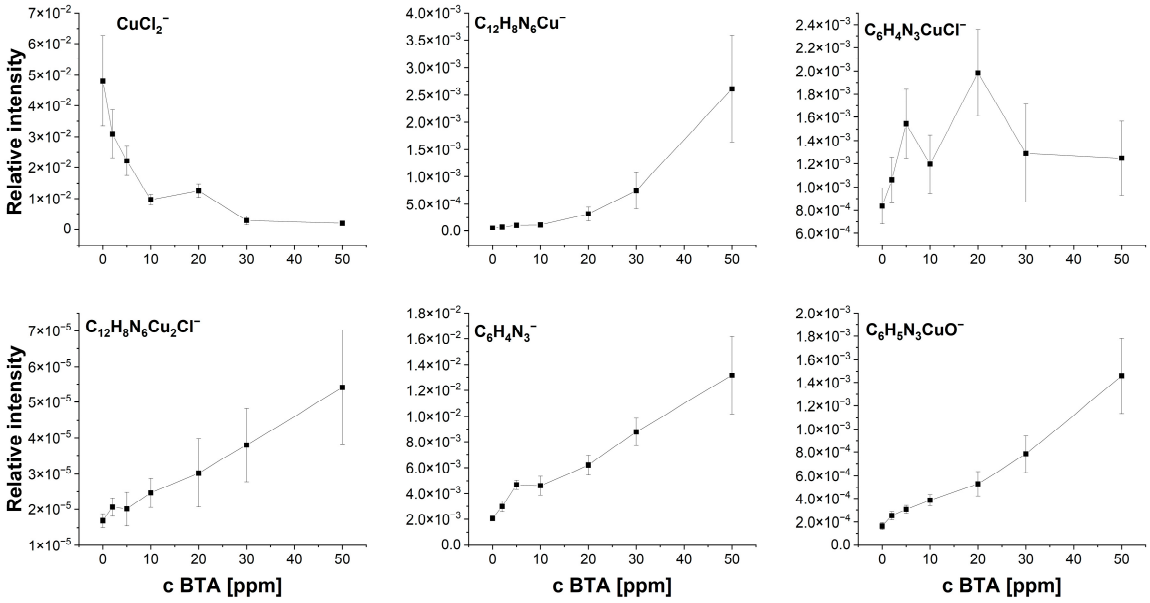


Figure 16. Distribution of intensity of the selected negative fragments: $CuCl_2^-$, $C_{12}H_8N_6Cu^-$, $C_6H_4N_3CuCl^-$, $C_{12}H_8N_6Cu_2Cl^-$, $C_6H_4N_3^-$, and $C_6H_4N_3CuOH^-$ on the copper surface obtained from solutions contained: 0, 2, 5, 10, 20, 30, and 50 ppm of BTA, and 30 ppm of Cl.

However, the fragment $C_6H_4N_3^-$ can be yielded from different parental forms of BTA, which makes the identification of the parental form on the copper surface more difficult. More informative fragments having a greater m/z value, such as $C_6H_4N_3CuOH^-$, stand for monomeric BTA in hydroxylated form that grows logarithmically as a function of BTA concentration from 2 to 20 ppm, while at greater BTA concentrations (30 and 50 ppm), they give rise in a more significant way. The intensity of the dimeric form, i.e., $C_{12}H_8N_6Cu^-$, is very low at BTA concentrations of 2, 5, and 10 ppm, while at 20, 30, and 50 ppm, it exponentially grows. It is the opposite situation that occurred in solution without chloride, in which the intensity of the dimeric form significantly grows at 5 and 10 ppm of BTA. It seems that chloride ions covering the copper surface inhibit the formation of BTA in its dimeric form. After the replacement of a significant amount of chloride ions directly bonded to the copper surface at 30 and 50 ppm by BTA molecules, the number of dimeric forms represented by the $C_{12}H_8N_6Cu^-$ fragment constantly grows. The possible Cu-BTA-Cl complex formation can be examined by the distribution of $C_6H_4N_3CuCl^-$ and $C_{12}H_8N_6Cu_2Cl^-$. A very high intensity of these

fragments was observed for samples 1 and 11 in the dip-coating experiment (Section 2.1). The abundance of $C_{12}H_8N_6Cu_2Cl^-$ constantly grows, similarly to that of $C_6H_4N_3CuOH^-$. However, at 50 ppm of BTA intensity, the distribution of $C_{12}H_8N_6Cu_2Cl^-$ is slightly different than other Cu-BTA complexes and demonstrates the highest yield around OCP (wire position 1.5 mm). It strongly suggests that the $C_{12}H_8N_6Cu_2Cl^-$ complex formation may be realized at greater surface coverage by chloride ions (2, 5, and 10 ppm of BTA) and at a lower amount of Cl directly bonded to the copper surface (30 and 50 ppm of BTA), as shown in Figure 17.

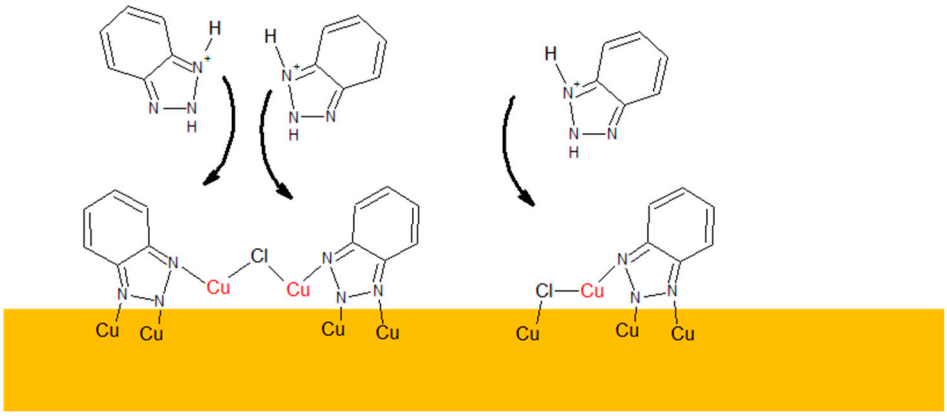


Figure 17. Proposed the cycle of BTA under the copper electrodeposition regime in the presence of chloride ions. The red color Cu stands for adatom. The orange color symbolizes the Cu layer.

The intensification of non-chloride $C_{12}H_8N_6Cu$ complex formation in solutions containing greater amounts of BTA (30 and 50 ppm BTA) but without chloride ions is clearly seen. In consequence, the coexistence of $C_{12}H_8N_6Cu_2Cl^-$ and $C_{12}H_8N_6Cu^-$ complexes at 30 and 50 ppm of BTA occurs.

The complex $C_{12}H_8N_6Cu_2Cl^-$ formation at 30 and 50 ppm of BTA can be followed via the following pathway:

$$2CuCl_2^{-} + 2\,C_6H_6N_3^{+} \rightarrow C_{12}H_8N_6Cu_2Cl^- + 3Cl^- + 4H^+ \quad (11)$$

On the other hand, at lower amounts of BTA (2, 5, 10, and 20 ppm), the complex can be formed by the reaction of BTA molecules and chloride ions adsorbed on the copper as follows:

$$2\,C_6H_4N_3^{\bullet}(ads) + 2Cu(ad) + Cl^-\,(ad) \rightarrow C_{12}H_8N_6Cu_2Cl^- \quad (12)$$

The formation of complex [Cu(I)ClBTAH]$_4$ was postulated by Rubim et al. [65] based on their SERS studies. However, as it was mentioned earlier, SERS does not provide direct identification of the molecular form of BTA-Cu-Cl complexes. Moreover, polymeric complexes in the form of Cu-BTA-Cl studied by XPS were postulated [90].

At greater amounts of BTA (30 and 50 ppm), dissociative adsorption of BTA in deprotonated form to the copper surface is more favorable than adsorption of chloride ions. On the other hand, the adsorption of chloride ions in the complexed form $C_{12}H_8N_6Cu_2Cl^-$ created in Reaction (1) simultaneously occurs. It arises from the fact that the protonated form of BTA is less hydrated than chloride ions.

The simplified pathway of reactions (11) and (12) is shown in Figure 17.

Different forms of Cu-BTA-Cl complexes may be assigned to $C_6H_4N_3CuCl^-$, whose intensity rises to 20 ppm of BTA (at 10 ppm, we observe its lower amount), while at 30 and 50 ppm, BTA significantly decreases. The distribution of $C_6H_4N_3CuCl^-$ in comparison to $CuCl_2^-$ demonstrates a reasonable correlation.

At 2 and 5 ppm, the ratio of $C_6H_4N^-/CuCl_2^-$ (Figure 15) is below 0.5 and is constant at wire position from 0 to 2100 µm, while the amount of $C_6H_4N_3CuCl^-$ constantly grows. For 10 ppm of BTA, the intensity of $C_6H_4N_3CuCl^-$ is significantly reduced due to the greater ratio $C_6H_4N^-/CuCl_2^-$. Subsequently, at 20 ppm of BTA, the $C_6H_4N^-/CuCl_2^-$ ratio gives

rise at wire positions 1300 to 2300 μm while the amount of $CuCl_2^-$ simultaneously grows. It means that a greater amount of BTA molecules and chloride ions at this BTA concentration is favorable for Cu-BTA-Cl complex formation. At the greatest BTA concentrations (30 and 50 ppm), the $C_6H_4N^-/CuCl_2^-$ ratio significantly grows, which determines the low amount of possible Cu-BTA-Cl complexes, as proven by the lower intensity of $C_6H_4N_3CuCl^-$. On the other hand, it is difficult to conclude that the fragment $C_6H_4N_3CuCl^-$ may exist in complex, parental form on the copper surface or be yielded via the reaction of copper sputtered ions during Bi primary beam bombardment. The replacement of chloride ions by BTA shown in Figure 15 is determined by the fact that chloride ions are smaller than BTA and solvate significantly stronger in water solutions than BTA^- [87]. In consequence, chloride ions lose competition in adsorption with BTA.

The $C_6H_4N_3CuCl^-$ complex formation is realized via the reaction of the protonated form of BTA with the $CuCl_2^-$ chloride complex.

$$CuCl_2^{-} + C_6H_6N_3^+ \rightarrow C_6H_4N_3CuCl^- + Cl^- + 2H^+ \quad (13)$$

Or alternatively, after adsorption of BTA on the copper, a chloride ion can be attached to the copper adatom.

$$C_6H_4N_3Cu\ (ads) + Cl^- \rightarrow C_6H_4N_3CuCl^- \quad (14)$$

Polymeric forms of Cu-BTA-Cl complexes were postulated previously for benzotriazole [90]. Furthermore, polymeric chloride complexes for 2-mercaptobenzimidazole (MBI) were also reported [91]. On the other hand, the occurrence of cuprous intermediates Cu^+/Cu(I)BTA/CuCl that partially eliminate the inhibition properties of BTA was recently postulated [20]. TOF-SIMS results show that chloride ions are connected to the BTA molecules through Cu^+ ions from the solution side and are not directly bonded to the copper substrate, as shown in Figure 17. It is supported by the very low intensity of $CuCl_2^-$, which stands for chloride ions in the form of CuCl, on the copper surface.

To reveal the formation of Cu-BTA-Cl complexes, we carried out SERS measurements (Section 2.10). The SERS technique can provide additional understanding about the mechanism of Cu-BTA-Cl complex formation.

The distribution of selected positive fragments as a function of BTA concentration is shown in Figure 18. The fragment Cu_2Cl^+ apparently shows a similar distribution as $CuCl_2^-$ and corresponds to the chloride ions on the copper surface.

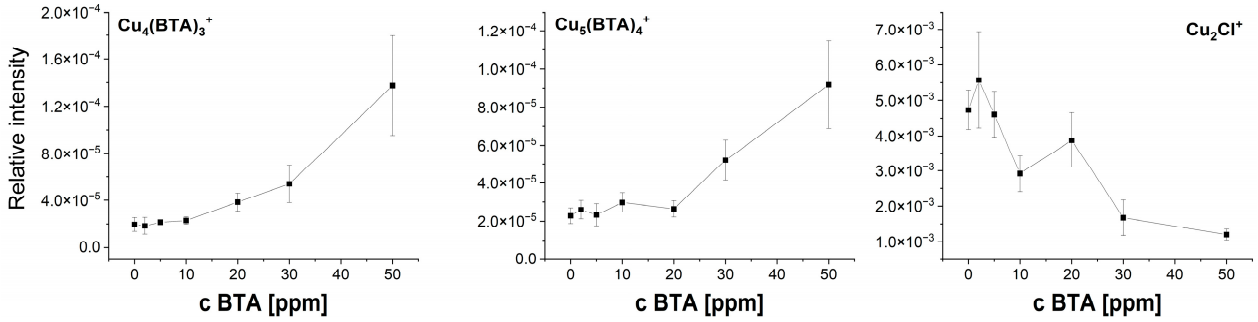


Figure 18. Intensity distribution of $Cu_4(BTA)_{3^+}$, $Cu_5(BTA)_{4^+}$, and Cu_2Cl^+ on the copper surface obtained from solutions contained: 0, 2, 5, 10, 20, 30, and 50 ppm of BTA, and 30 ppm of Cl^-.

The distribution of $Cu_4(BTA)_{3^+}$ is very similar to that of the negative fragment $C_{12}H_8N_6Cu^-$. It means that these two fragments correspond to a similar parental molecular arrangement. It supports the proposed $Cu_4(BTA)_{3^+}$ molecular structure (Figure 2), in which the central copper core is covered by the BTA-Cu-BTA and one free BTA molecule. On the other hand, binding of BTA-Cu-BTA and two BTA molecules to the copper core in the form $Cu_5(BTA)_{4^+}$ is possible only at 30 and 50 ppm of BTA if all chloride ions are removed from the copper surface. No chloride complexes such as $Cu_4(BTA)_3CuCl^+$

with mass 705.80 identified in the dip-coating experiments (Section 2.1) for samples 1 and 11 were observed in the positive ion mode mass spectra. It means that such complexes can be formed in bulk solutions under chemical conditions in less acidic solutions, as was conducted in the dip-coating experiment.

2.8. Incorporation of BTA into Copper during Copper Electrodeposition from Electrolyte Containing BTA with Chloride Ions—TOF-SIMS Measurements

The incorporation of the selected monomeric, dimeric, trimeric, tetrameric, and pentameric forms into the copper deposit is shown in Figure 19. It is clearly seen that for 50 ppm of BTA with chloride ions (right side of plot), the contribution of the incorporated dimeric copper complex form $C_{12}H_8N_6Cu^-$ in relation to the monomeric form $C_6H_4N_3CuOH^-$ is higher than it was in BTA without Cl (left plot). Moreover, the amount of incorporated polymeric $Cu_4(BTA)_{3^+}$ and $Cu_5(BTA)_{4^+}$ forms is also greater than it was without chloride ions. It means that chloride ions stabilize the incorporation of organometallic complexes of BTA into deposits. It can be determined by the lower mobility of the Cu-BTA complexes in the presence of Cu-BTA-Cl. Moreover, the surface roughness in the presence of chloride ions may significantly change, which may increase the adsorption energy of copper metallic complexes in situations where the number of coordinated copper atoms decreases [28,87]. Surface roughness with and without chloride ions was examined by atomic force microscopy (Section 2.11).

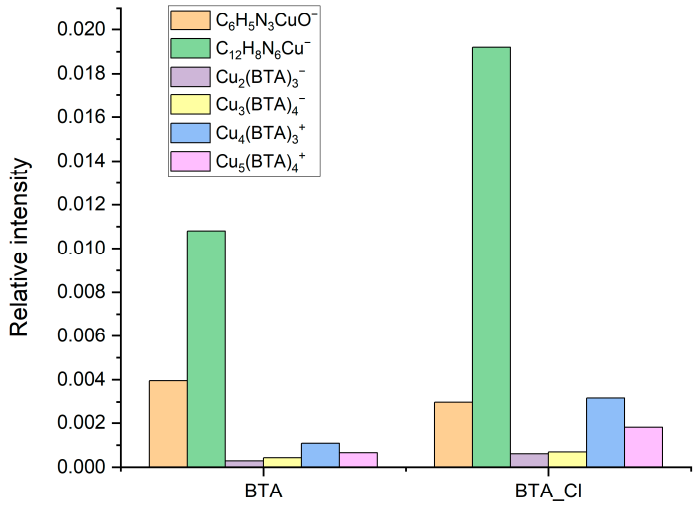


Figure 19. Intensity distribution of $C_6H_4N_3CuOH^-$, $C_{12}H_8N_6Cu^-$, $Cu_2(BTA)_{3^-}$, $Cu_3(BTA)_{4^-}$, $Cu_4(BTA)_{3^+}$, and $Cu_5(BTA)_{4^+}$ on the copper surface after etching in nitric acid. For BTA 50 ppm and chloride ions (right plot). For comparison, the same fragments for BTA at 50 ppm without chloride ions are shown on the left side.

Overall, in the presence of chloride ions, BTA molecules are incorporated into copper deposits similarly to what was shown in Figure 12. While partial desorption of incorporated BTA into copper deposits was postulated previously [21]. Incorporation of BTA molecules and chloride ions by examination of Cl and S by means of TOF-SIMS in dynamic mode was carried out previously [77].

2.9. Distribution of BTA and Micromorphology of Copper Surface Obtained from Electroplating Bath with Chloride Ions

Figure 20 depicts the distribution of the total ion image, $C_6H_4N_{3^-}$, and the backscattered secondary electron image. The darker areas in the total ion image correspond to the low amount of BTA ($C_6H_4N_{3^-}$).

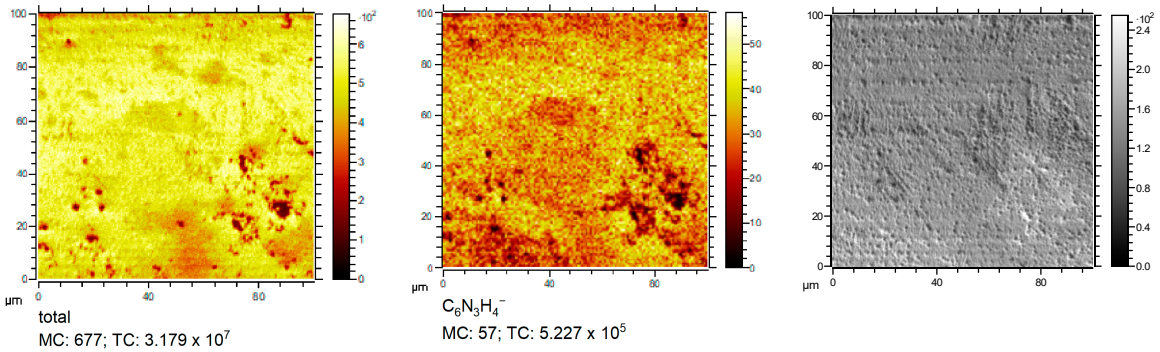


Figure 20. Distribution of total ion image (left) and $C_6H_4N_{3^-}$ (middle) for BTA 50 ppm/Cl 30 ppm at wire position 1900 µm. Scanning area: 100 × 100 µm. The right column image shows a backscattered secondary electron image with a resolution of 0.2 µm. The dark areas in the total ion image correspond to the low amount of BTA as depicted by the $C_6H_4N_{3^-}$ ion distribution. The dark areas in the total ion image and $C_6H_4N_{3^-}$ correspond to the crystals visible in the SE image.

The secondary electron image (right image) shows that crystals appear in areas corresponding to very low BTA surface coverage. Such observations were also noticed for BTA without chloride. It proves the inhibition properties of BTA in suppressing copper crystal growth at the microscale. Investigation of BTA influence on surface morphology at the nanoscale for all BTA concentrations in the presence of chloride ions was examined by AFM (results and discussion in Section 2.11).

2.10. Chemistry of Copper Surface Deposited from Electrolytes Containing BTA with Chloride Ions—SERS Studies

After the addition of chloride ions, a few significant differences in the SERS spectra in comparison to the samples without chloride ions (Section 2.7) can be observed (Figure 21).

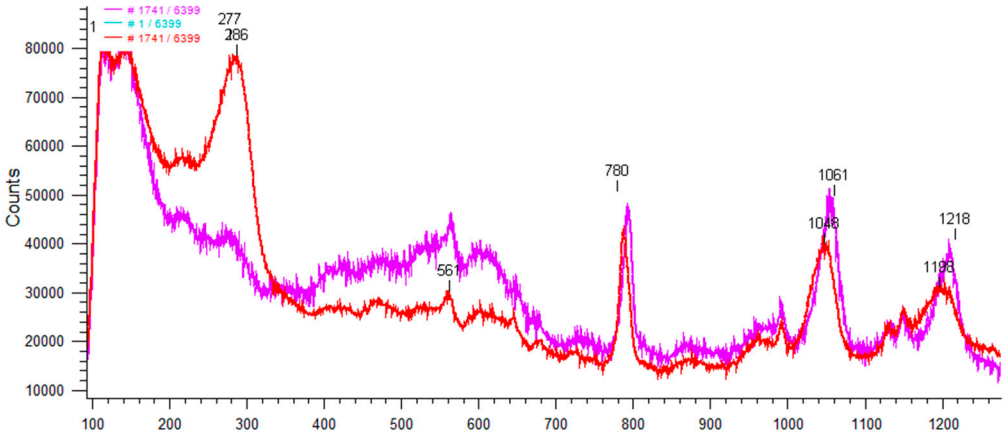


Figure 21. SERS spectra for BTA without chloride ions (pink) and with chloride ions (red color).

A strong, wide band at 280 cm^{-1} corresponds to the Cu-Cl bond [92]. Moreover, the bands 795 cm^{-1} and 1053 cm^{-1} are slightly redshifted, c.a. 3 cm^{-1}. The intensity of the band 1053 cm^{-1} is significantly reduced, and the peak is broadened. Furthermore, the band 1209 cm^{-1} characteristic for the molecular form of BTAH corresponds to the adsorbed BTA molecules on metallic copper and is significantly reduced and redshifted to 1193 cm^{-1}. The distribution of bands 300 cm^{-1} and 800 cm^{-1} at 0, 2, 10, 20, 30, and 50 ppm of BTA with the presence of 30 ppm chloride ions along the wire position is shown in Figure 22.

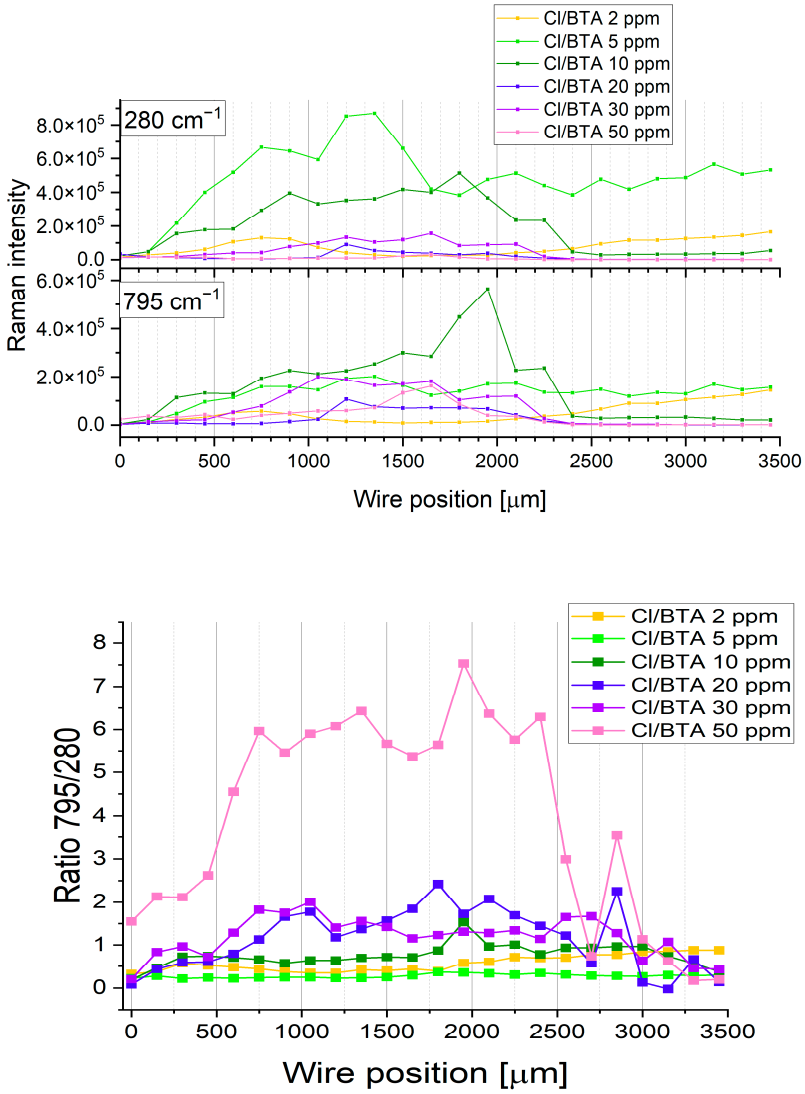


Figure 22. Distribution of Raman intensity for bands 280 cm^{-1}, 795 cm^{-1}, and the ratio bands 795/280 along wire position for 2, 5, 10, 20, 30, and 50 ppm of BTA in the presence of Cl (30 ppm) in the solution that shows chloride replacement by BTA molecules (see for comparison Figure 15 that presents a similar effect examined by TOF-SIMS).

Raman intensity of band 280 cm^{-1} is not inversely proportional to the BTA concentration as it was observed for TOF-SIMS (see Figures 15 and 16, $CuCl_2^-$, and Figure 18 Cu_2Cl^+). We should expect the greatest Raman intensity for the Cu-Cl bond at 0 ppm of BTA, whereas the lowest is at 50 ppm of BTA. As it is seen in Figure 22, the greatest SERS intensity is observed at 5 ppm of BTA, while the lowest is at 50 ppm. It arises from the fact that the SERS signal is very sensitive to the surface roughness [84,85] and thickness of the layer, as shown in Section 2.5.

Similarly, for band 795 cm^{-1} (benzene ring breathing in BTA), one can observe the greatest Raman intensity increases for BTA concentrations from 2 to 10 ppm, while for greater BTA amounts, the Raman signal is significantly reduced in rather random order. It is contrary to the TOF-SIMS, with the intensity of fragments characteristic for BTA proportionally increasing with the BTA amounts in the solution (Figures 15, 16 and 18). Figure 22 (bottom plot) shows the ratio of bands 795/280 for 0, 2, 10, 20, 30, and 50 ppm of BTA that corresponds to the ratio BTA/Cl on the copper surface and illustrates the replacement of chloride ions by BTA molecules.

The ratio 795/280 slowly increases for BTA concentrations from 2 to 10 ppm. Subsequently, significant increases occurred for 20 and 30 ppm of BTA. For the highest BTA amount (50 ppm), the ratio is very high (about 6) in comparison to the rest of the samples. It may suggest that all chloride ions are replaced by BTA molecules.

To estimate possible forms of BTA (molecular or complex) on the copper, we calculated the 1208/1190 ratio similarly to how it was conducted for BTA without chloride ions (Figure 23).

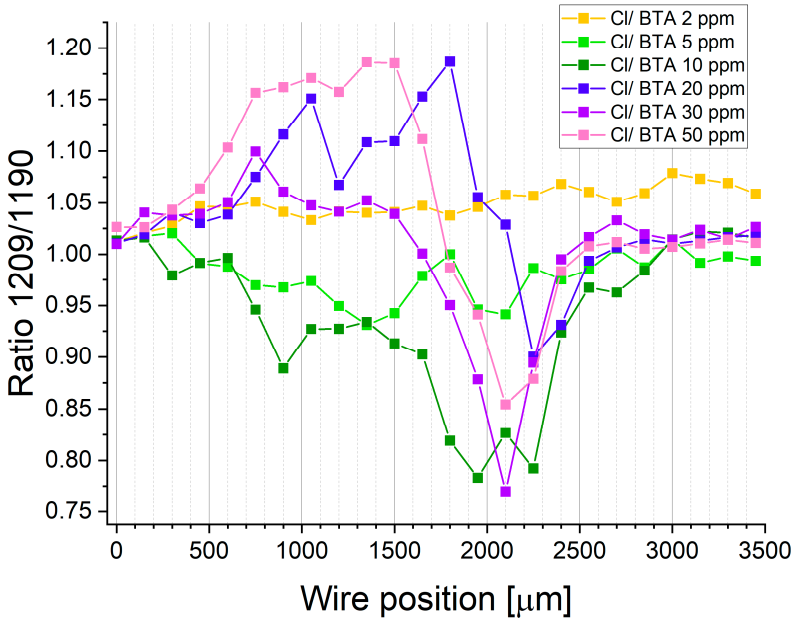


Figure 23. Ratio of intensity bands 1208/1190 for different BTA concentrations.

At 2 ppm of BTA, the 1208/1190 ratio is constant for the whole potential range. It means that the shape of band 1028 cm^{-1} is not changing and that BTA exists only in molecular form. For 5 and 10 ppm of BTA, the ratio 1208/1190 diminishes for forward scan (wire position 0–1500 μm). For reverse scan, for 5 ppm, the ratio 1208/1190 is varied, while for 10 ppm of BTA, it is further reduced up to wire position 2300. When the SERS signal is significantly reduced (wire position 2400–3500 μm), the ratio 1208/1190 for 10 ppm of BTA increases. It may suggest that for high overpotentials of reverse scanning when strong desorption of BTA and Cl ions occurs, the molecular form of BTA dominates over the complex form of BTA due to the dissolution of the Cu(I)BTA complex by hydrogen ions.

A similar observation for high overpotential was previously noticed for BTA on copper surfaces in sulfuric acid [63]. For 30 ppm of BTA, the ratio 1208/1186 is rather constant for the forward scan, while for 20 and 50 ppm of BTA, it is significantly higher. After switching the sweep direction from anodic to cathodic, the ratio 1208/1190 significantly diminishes for 20, 30, and 50 ppm of BTA up to wire position 2100–2300 μm. It corresponds to the region when the SERS signal is strongly reduced (Figure 22). Overall, only for 2 and 5 ppm of BTA, we could not observe such a significant decrease in the ratio 1208/1190. However, for these samples, the Raman signal does not decrease at the wire position from 2400 to 3500 μm. Moreover, we can conclude that the ratio of the molecular form of BTA to the complex form, expressed as a ratio of 1208/1190, dominates for BTA at 20 and 50 ppm, while the complex form may coexist with the molecular form at 5 and 10 ppm for forward scanning.

The Cu(I)BTACl complex formation can be driven by the coexistence of Cl and BTA species as well as the optimal molar ratio of BTA/Cl on the copper surface. The existence of the complex form Cu(I)BTACl is noticed at low ratios of BTA/Cl observed for 5 and 10 ppm of BTA (ratio 795/280, Figure 22).

On the other hand, at a lower amount of BTA (2 ppm), the Cu-Cl complex formation dominates, and the formation of the Cu-BTA-Cl complex does not occur. For BTA concentrations greater than 10 ppm, the ratio BTA/Cl significantly increases (Figure 22), which

shows a reduced available number of chloride ions near the BTA molecules, remarkably decreasing the probability of Cu-BTA-Cl complex formation.

However, the SERS data does not support the existence of complex forms for concentrations greater than 20 ppm of BTA. On the other hand, the existence of $C_{12}H_8N_6Cu_2Cl^-$ was proven by TOF-SIMS, which provides direct information about molecular species in contrast to the SERS, where assignments of bands are very often not certain and the abundance of different bands is very sensitive to the surface roughness and thickness of the deposited layer, as shown in Section 2.5 and in this section.

2.11. Surface Morphology at the Nanoscale—Atomic Force Microscopy Measurements

The micrographs of the copper surface obtained with the presence of BTA in the electroplating solution without chloride ions are shown in Figure 24.

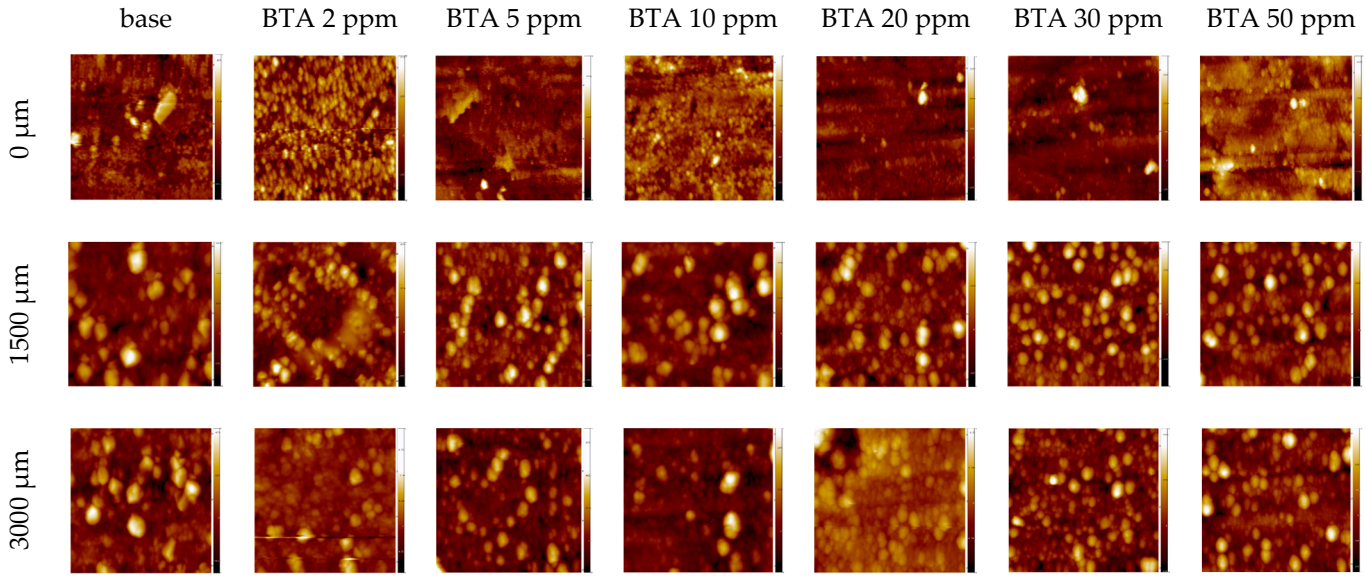


Figure 24. AFM micrographs of copper surfaces electrodeposited from solution contained: 0, 2, 5, 10, 20, 30, and 50 ppm of BTA at wire positions of 0, 1500, and 3000 µm. Moreover, 0 µm corresponds to the copper surface at the starting point of the cyclic voltammetry experiment (potential −0.6 V forward scan), position 1500 µm corresponds to the OCP, and 3000 µm corresponds to the −0.6 V overpotential—reverse scan. Scanning area: 20 × 20 µm.

Position 0 µm corresponds to the starting point of the CV experiment at an overpotential −0.6 V. The copper layer was obtained at this point by electrodeposition at a constant current density −15 mA/cm^2 for 120 s. The surface roughness parameter (Sq) is included in Table 4.

Table 4. Surface roughness (Sq) determined for copper layer obtained from solution containing 0, 2, 5, 10, 20, 30, and 50 ppm of BTA at wire positions: 0, 1500, and 3000 µm.

Wire Position	Base	BTA 2 ppm	BTA 5 ppm	BTA 10 ppm	BTA 20 ppm	BTA 30 ppm	BTA 50 ppm
0 µm	79.124	52.454	33.264	34.067	42.567	49.747	45.719
1500 µm	140.19	96.149	87.30	130.58	95.958	80.233	83.440
3000 µm	100.76	96.564	91.148	87.468	118.87	81.827	82.237

After the addition of 2 ppm BTA, roughness is significantly reduced from 79 nm to 52 nm. The roughness obtained for 2 and 5 ppm of BTA was remarkably lower than for 20, 30, and 50 ppm of BTA. It seems that the lower levels of BTA molecules on the copper and into the copper deposit observed at 2 and 5 ppm demonstrate the strongest

inhibiting properties for copper crystal growth. At higher amounts of BTA (10, 20, 30, and 50 ppm), the excess of accumulated BTA dimeric and polymeric forms perturbs the diffusion control of copper ions onto the copper surface. Moreover, polymeric complexes of $Cu_4(BTA)_{3^+}$ and $Cu_5(BTA)_{4^+}$ identified in the TOF-SIMS spectra consist of core copper clusters that can induce agglomeration of copper adatoms. Similar effects can occur for dimeric and linear forms of Cu-BTA complexes. During the CV experiment (positions 1500 and 3000 µm), roughness rapidly grows, while under the OCP condition (wire position 1.5 mm), the lowest roughness is observed for 30 and 50 ppm of BTA. Rapid growth of surface roughness during the CV experiment is determined mainly by the fact that at high overpotential conditions during forward scanning, BTA is not present or occurs in very low amounts on the surface (notice TOF-SIMS data, Figure 5). Under these circumstances, copper grain growth is not inhibited. It means that BTA influence on the morphology strongly depends on applied overpotential. During reverse scan at −0.6 V (wire position 3000 µm), for low BTA concentrations (2 and 5 ppm) and the greatest (30 and 50 ppm), the surface roughness is maintained, while for 10 and 20 ppm, it is varied. Similarly to the results we observed at the 0 µm wire position, copper electrodeposited from solutions consisting of BTA demonstrated significant brightening abilities in comparison to the base electrolyte [21–23,66].

After the addition of chloride ions, surface morphology significantly changes (Figure 25). At wire position 0 µm, which corresponds to the copper electrodeposited at −15 mA/cm^2, the surface contains numerous crystallites from the base electrolyte and roughness at a level of 35 nm (Table 5). After injection of chloride ions, the surface considerably refines to develop a noninotropic structure with large flat terraces (Sq = 41 nm). After the addition of BTA (2 ppm), a significant number of small grains appear on the surface while roughness increases. The next portion of BTA (5 ppm) determines the increasing size of copper protrusions. In consequence, the surface roughness increases (Sq = 100 nm). At 10 ppm of BTA, due to the significant replacement of chloride ions (see TOF-SIMS results) by BTA molecules, the process of grain growth is inhibited and roughness is reduced (Sq = 67 nm). For 20 ppm, the characteristic lamellar forms appear with a lower diameter than the grains noticed at 10 ppm BTA. In effect, a lower roughness (54 nm) was observed. The process is constantly intensified at 30 ppm of BTA, where lamellar forms demonstrate smaller diameters and lower surface roughness (38 nm). At the greatest BTA amount (50 ppm), lamellar forms disappear (Sq = 41 nm). During the CV experiment under the OCP regime (wire position 1500 µm), surface roughness dramatically increased for all samples (Table 4). All characteristic features distinguished on the copper surface at position 0 µm are also observable and growing. A similar effect is observed at the greatest overpotential for reverse scan (−0.6 V, wire position 3000 µm). In the latter case, it is obvious that the time of electroplating during the CV experiment (30 s from OCP to −0.6 V) is not sufficient to refine the morphological structure of the copper deposit determined at OCP. On the other hand, during the same time electrodeposition, the potential sweep from −0.6 V to OCP (wire position from 0 to 1500 µm) changes the morphology and structure. It seems that the formation of the complex Cu-BTA-Cl identified in the TOF-SIMS spectra is responsible for the significant structure changes. Characteristic lamellar structures at 20, 30, and 50 ppm were formed as a significant amount of the chloride complex $C_{12}H_8N_6Cu_2Cl^-$ was identified (see Section 2.7).

Table 5. Surface roughness (Sq) determined for copper layer obtained from solution containing: 0, 2, 5, 10, 20, 30, and 50 ppm of BTA with the presence of 30 ppm of chloride ions at wire positions: 0, 1500, and 3000 µm.

Wire Position	Base	Cl 30 ppm	Cl_BTA 2 ppm	Cl_BTA 5 ppm	Cl_BTA 10 ppm	Cl _BTA 20 ppm	Cl_BTA 30 ppm	Cl _BTA 50 ppm
0 µm	35.409	41.525	60.579	100.76	67.580	53.984	38.826	41.014
1500 µm	142.89	245.31	217.50	191.20	162.27	126.51	145.92	167.15
3000 µm	134.38	252.31	252.33	183.81	202.65	209.98	153.11	127.71

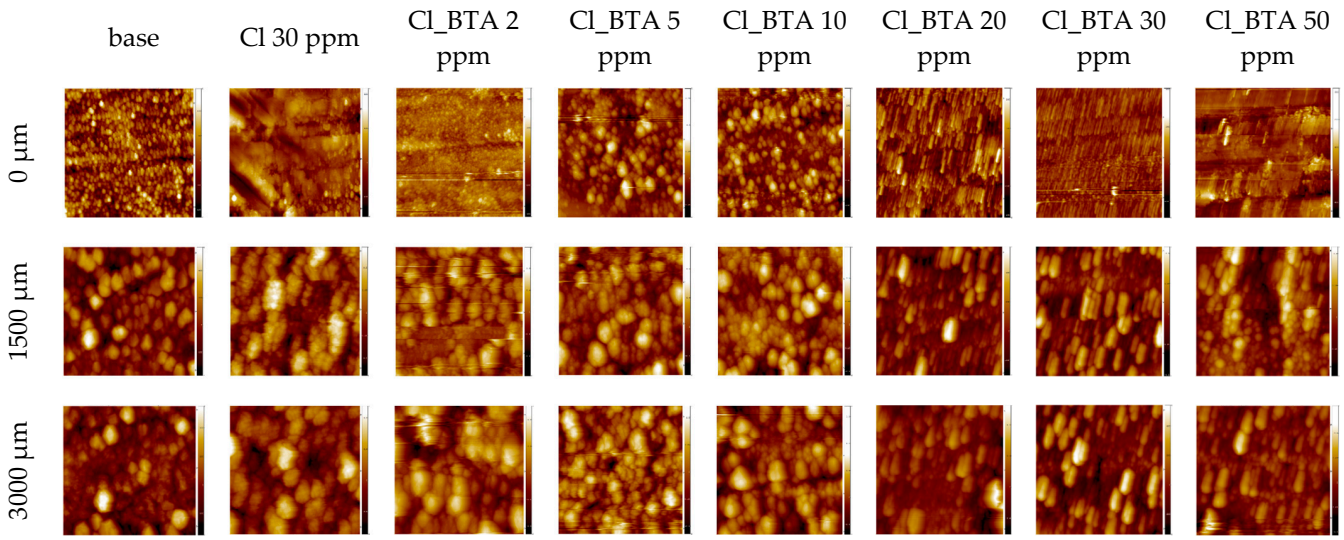


Figure 25. AFM micrographs for copper surfaces electrodeposited from solution contained: 0, 2, 5, 10, 20, 30, and 50 ppm of BTA and 30 ppm of chloride ions at wire positions of 0, 1500, and 3000 µm. Moreover, 0 µm corresponds to the copper surface at the starting point of the cyclic voltammetry experiment (potential −0.6 V, forward scan); position 1500 µm corresponds to the OCP; and 3000 µm corresponds to the −0.6 V overpotential, reverse scan. Scanning area: 20 × 20 µm.

Evaluation of surface roughness for 10 µm thick of copper deposited from solutions BTA (12 ppm) and BTA (12 ppm)/Cl^- (10 ppm) at −40 mA/cm^2 at a rotating speed of 5000 rpm showed [21] that after addition of Cl^- ions, roughness rapidly grows. In our experimental conditions at a comparable molar ratio of BTA (30 ppm)/Cl^-(30 ppm), we observed that roughness is lower than it was for BTA (30 ppm) only. However, we electrodeposited copper at a lower current density (i.e., −15 mA/cm^2), the electroplating bath was not stirred, and the thickness was around 2 µm.

3. Materials and Methods

The dip-coating experiment (Section 2.1) was carried out in a test tube containing 10 mL of electrolyte. During a dip-coating experiment, 20 samples were prepared (Table 1). The nitinol wire (assigned as Sample 1, NiTi) was immersed for 60 s in a solution containing 0.1 M BTA/6.25mM $CuCl_2$ and then withdrawn at a constant speed of 1 mm/s and dried in the air at room temperature. The next sample (2, NiTi/rinsing) was prepared in the same way, but after deposition, it was rinsed in a 5% ethanol solution. The procedure for rinsing was described in the experimental section. Similarly, the subsequent nitinol samples were prepared in the same way, while the composition of additives varied. The same procedure of deposition was applied to the nitinol wires with a pre-plated copper layer.

Samples were assigned as: NiTi; NiTi/rinsing; Cu; Cu/rinsing; Cu; and Cu/rinsing, depending on the method of preparation.

The base electrolyte contained sulfuric acid (99.9% pure, POCH S.A., Gliwice, Poland) and copper sulfate (99% pure, Supelco, Bellefonte, PA, USA). The following additives were added: Cl^- (in the form of HCl, POCH S.A., Gliwice, Poland) and benzotriazole (99% pure, Sigma-Aldrich, Saint Louis, MO, USA). For the preparation of all solutions, deionized water (18 MΩ, Hydrolab, Straszyn, Poland) was applied. For cyclic voltammetry experiments (CV), a 120 mm piece of superelastic nitinol wire (0.665 mm diameter, Ni—55%, Ti—45%, supplied by Euroflex GmbH, Pforzheim, Germany) was immersed in a copper sulfate solution for a length of 50 mm (1 cm^2 surface area).

Cyclic voltammetry (CV) experiments were accompanied by TOF-SIMS experiments, and a copper ring with phosphor as an additive (45 mm outside and 30 mm internal diameter, 1 mm thickness, supplied by Lesker, Jefferson Hills, PA, USA) was employed as counter electrodes and mounted on the bottom of the test tube. The tube contained

250 mL of the electroplating bath. The purity and manufacturer of components of the electroplating bath were mentioned above, while the concentration of the base solution (without additives) was as follows: $CuSO_4$* × $5H_2O$—0.225 M, sulfuric acid—0.56 M. Accordingly, benzotriazole at concentrations of 0, 2, 5, 10, 20, 30, and 50 ppm without and with Cl^- ions, at a concentration of 30 ppm, was added.

A counter-electrode was connected to a galvanostat using a copper wire (diameter 1 mm) covered by a thick isolated lacquer layer, resisting the electroplating bath. As a reference electrode, an $Ag/Ag_2SO_4/(sat.)K_2SO_4$ electrode (Eurosensor, Gliwice, Poland) was applied. Reference potential (vs. SCE) was equal to +0.163 V (according to the manufacturer's statement). A galvanostat AUTOLAB 302N (Eco Chemie, Utrecht, The Netherlands) and software NOVA 1.11 (Methrohm, Utrecht, The Netherlands) were employed for cyclic voltammetry (CV) experiments. The ohmic overpotential estimated at 10 Ω during CV scans was not corrected. Before the addition of sulfuric acid and additives, the copper sulfate solution was thoroughly deoxygenated using an ultrasonic washer under reduced pressure. The conductivity of the base solution was equal to 208 $mScm^{-1}$ at pH 1.05, respectively. The solution temperature was equal to 23 °C. The electroplating bath was not stirred. Before each experiment, the counter-electrode was immersed in fresh 30% HNO_3 for 30 s, then thoroughly rinsed in deionized water and dried in the air. Subsequently, nitinol wire, which served as a working electrode, was mounted vertically in the electroplating bath, and copper was electrodeposited at a constant current density −15 mA/cm^2 for 120 s. After copper preplating, nitinol wire with a copper layer was withdrawn at a constant speed equal to 34 μm/s from the copper electroplating bath under electrodeposition conditions by means of an upright-mounted motorized ES111 OptiScan stage (Prior Scientific Instruments Ltd., Cambridge, UK) Simultaneously, the CV experiment was performed, and the applied potential was swept at constant velocity, V = 20 mV/s, in the range of overpotential between −0.6 V and OCP (forward scan to anodic direction) and from OCP to −0.6 V (reverse scan to cathodic direction), where OCP is an open circuit potential. OCP was determined for 120 s or less before the CV experiment on the copper preplated layer until a steady state was reached. In this manner, during a CV experiment, one cyclic loop corresponds to 60 s (30 s for the forward scan in the anodic direction and 30 s for the reverse scan in the cathodic direction) and 2 mm of the nitinol wire (working electrode) length during a withdrawal. The forward scan from −0.6 V to OCP corresponds to the wire position from 0 to 1000 μm, while the reverse scan corresponds to the position from 1000 to 2000 μm, respectively. An additional scheme of the CV experiment is shown in Figure S3 (Supplement Materials). To avoid copper sulfate salting out, an optimized method of rinsing was applied. More details on the rinsing method can be found elsewhere [19]. Briefly, a glass capillary with an internal diameter of 2.4 mm was immersed in a rinsing solution (5% aquatic ethanol) and mounted horizontally. Deionized water for preparing the rinsing solution (5% aquatic ethanol) was boiled to remove carbon dioxide, which may increase the solubility of the examined solid films adsorbed on the copper surface during electrodeposition. The total volume of rinsing solution inside the capillary was 8 μL (height of rinsing liquid: ~1 mm) and was collected at the bottom end of the capillary. The rinsing properties of 5% ethanol in deionized water and other concentrations of ethanolic solutions were determined in previous work [43].

After preparation, samples were transferred to the TOF-SIMS vacuum chamber and routinely measured not later than 2–5 h after preparation. TOF-SIMS spectra were acquired by means of the TOF-SIMS.5 instrument (ION-TOF GmbH, Münster, Germany). The primary ion source of Bi^+ was used at 30 keV (cyclic time 100 μs, primary beam current 1.2 pA). The scanning area of the secondary ions was 50 × 50 μm with 128 × 128 pixels and 1 shot/pixel. All the measurements were performed in a static mode (dose no larger than 1×10^{12} ions/cm^2) in a negative mode. For most of the samples, 30 or more points separated by 0.1 mm were measured. The post-processing data analysis was conducted using the SurfaceLab 6.7 software (ION-TOF) and Origin 2019 (OriginLab, Northampton,

MA, USA). The negative spectra were recorded and calibrated using the positions of CH^-, CH_{2^-}, and CH_{3^-}. Intensities were normalized to the total intensity.

After TOF-SIMS measurements, samples were taken for SERS measurements. SERS spectra were acquired by means of Raman via microscopy (Renishaw, Sheffield, UK). Measurements were carried out using a 785 nm laser source with a power of 50 mW on the sample (100% power), an exposure time of 50 ms, and one acquisition in StreamLineHR image acquisition mode with a step of 5um with an Andor detector. Objective 50× was carried out. The post-processing data analysis was conducted using the Wire 4.3 software (Renishaw) and Origin 2019. Subsequently, samples were transferred for atomic force microscopy. Measurements were carried out by atomic force microscopy with an Agilent 5600LS (Santa Clara, CA, USA) in tapping mode with a silicon tip (radius 7 nm). The data were evaluated using SPIP 5.1.4 (Image Metrology, Kongens Lyngby, Denmark).

4. Conclusions

In this paper, we examined for the first time the influence of benzotriazole on the copper electrodeposition with and without the presence of chloride ions by combining studies of cyclic voltammetry, TOF-SIMS, SERS, and AFM.

The obtained results show that benzotriazole, after dissociative adsorption to the copper surface, reduces current density in a logarithmic way as a function of BTA concentration for the studied concentration range of 2 to 50 ppm.

It was identified that the characteristic Cu-BTA fragments exist in negative and positive modes. The most prominent forms of Cu-BTA adducts identified in the negative mode correspond to the monomeric hydroxylated form of Cu-BTA in the form of $C_6H_4N_3CuOH^-$, the dimeric organometallic complex consisting of copper adatom, $C_{12}H_8N_6Cu^-$, and the trimeric form, $C_{18}H_{16}N_9Cu_{2^-}$. All forms identified in the negative modes demonstrate linear structure. In the positive mode, the trimeric and tetrameric forms $Cu_4(BTA)_{3^+}$ and $Cu_5(BTA)_{4^+}$ exist in cyclic forms that surround the central copper core.

In the presence of chloride ions at a concentration of 30 ppm, the inhibiting properties of BTA diminish due to the existence of Cl ions on the copper surface. Chloride ions are gradually desorbed. At BTA concentrations of 30 and 50 ppm, no chloride ions were directly adsorbed on the copper surface, while Cu-BTA-Cl complex formation was proven by TOF-SIMS and indirectly by SERS studies. The Cu-BTA-Cl complex was identified in the form of $C_{12}H_8N_6Cu_2Cl^-$ and $C_6H_4N_3Cu(I)Cl$. We proposed a scheme of formation for the Cu-BTA-Cl complexes.

Incorporation of BTA molecules into copper deposits, mainly in dimeric and polymeric forms, was proven for BTA with and without chloride ions in the electroplating bath.

It was also shown that the distribution of BTA spices on the copper electrode correlates with the microroughness of copper surfaces identified by backscattered electrons.

Roughness at the nanoscale was examined by atomic force microscopy and showed the existence of a specific lamellar structure on the copper surface in the presence of chloride ions. However, the structure strongly depends on the applied potential and composition of the electroplating solution.

Supplementary Materials: The following supporting information can be downloaded at: https://www.mdpi.com/article/10.3390/molecules28155912/s1.

Author Contributions: Conceptualization, R.M.; methodology, R.M.; formal analysis, R.M. and A.S.; investigation, R.M. and A.S.; data curation, R.M. and A.S.; writing—original draft preparation, R.M.; writing—review and editing, R.M. and A.S.; visualization, R.M. and A.S.; supervision, R.M.; All authors have read and agreed to the published version of the manuscript.

Funding: This research received no external funding.

Institutional Review Board Statement: Not applicable.

Informed Consent Statement: Not applicable.

Data Availability Statement: The TOF-SIMS, AFM, CV, and Raman data can be obtained upon reasonable request.

Acknowledgments: As the authors, we would like to thank Agata Ładniak for carefully reading the whole manuscript and for her fruitful tips.

Conflicts of Interest: The authors declare no conflict of interest.

Sample Availability: Samples of the compounds are not available from the authors.

References

1. Gagnard, X.; Mourier, T. Through Silicon via: From the CMOS Imager Sensor Wafer Level Package to the 3D Integration. *Microelectron. Eng.* **2010**, *87*, 470–476. [CrossRef]
2. Vereecken, P.M.; Binstead, R.A.; Deligianni, H.; Andricacos, P.C. The Chemistry of Additives in Damascene Copper Plating. *IBM J. Res. Dev.* **2005**, *49*, 3–18. [CrossRef]
3. Andricacos, P.C.; Uzoh, C.; Dukovic, J.O.; Horkans, J.; Deligianni, H. Damascene Copper Electroplating for Chip Interconnections. *IBM J. Res. Dev.* **1998**, *42*, 567–573. [CrossRef]
4. Moffat, T.P.; Josell, D. Superconformal Electrodeposition for 3-Dimensional Interconnects. *Isr. J. Chem.* **2010**, *50*, 312–320. [CrossRef]
5. Sulka, G.D. Electrochemistry of Thin Films and Nanostructured Materials. *Molecules* **2023**, *28*, 4040. [CrossRef]
6. Ahn, J.; Hong, S.; Shim, Y.-S.; Park, J. Electroplated Functional Materials with 3D Nanostructures Defined by Advanced Optical Lithography and Their Emerging Applications. *Appl. Sci.* **2020**, *10*, 8780. [CrossRef]
7. Sun, Z.; He, G.; Zhao, Z.; He, X.; Zhao, H. Research Progress of Electroplated Micropore for Interconnection Technology. *J. Phys. Conf. Ser.* **2023**, *2430*, 012011. [CrossRef]
8. Finšgar, M. The influence of the amino group in 3-amino-1,2,4-triazole corrosion inhibitor on the interface properties for brass studied by ToF-SIMS. *Rapid Commun. Mass Spectrom.* **2021**, *35*, e9056. [CrossRef]
9. Soares, D.; Wasle, S.; Weil, K.; Doblhofer, K. Copper Ion Reduction Catalyzed by Chloride Ions. *J. Electroanal. Chem.* **2002**, *532*, 353–358. [CrossRef]
10. Doblhofer, K.; Wasle, S.; Soares, D.M.; Weil, K.G.; Weinberg, G.; Ertl, G. The Influence of Halide Ions on the Kinetics of Electrochemical Copper(II) Reduction. *Z. Phys. Chem.* **2003**, *217*, 479–492. [CrossRef]
11. Hoang, V.H.; Yokoi, M.; Kondo, K. Kinetic on Copper Damascene and Cuprous Concentration Computation in with Cl—and SPS. *ECS Meet. Abstr.* **2015**, *MA2015-02*, 863. [CrossRef]
12. Xiang, J.; Qin, Z.; Xu, Y.; Zeng, C.; Yang, W.; Tian, L.; Ruan, H. Effect of Cu(I) on Electrochemical Behavior and Surface Morphology of Electrodeposited Copper for Different Accelerators. *Ionics* **2023**, *29*, 1487–1495. [CrossRef]
13. Broekmann, P.; Fluegel, A.; Emnet, C.; Arnold, M.; Roeger-Goepfert, C.; Wagner, A.; Hai, N.T.M.; Mayer, D. Classification of Suppressor Additives Based on Synergistic and Antagonistic Ensemble Effects. *Electrochim. Acta* **2011**, *56*, 4724–4734. [CrossRef]
14. Jin, Y.; Sui, Y.; Wen, L.; Ye, F.; Sun, M.; Wang, Q. Competitive Adsorption of PEG and SPS on Copper Surface in Acidic Electrolyte Containing Cl^-. *J. Electrochem. Soc.* **2013**, *160*, D20–D27. [CrossRef]
15. Mroczka, R.; Słodkowska, A.; Ładniak, A. Studies of Bis-(Sodium-Sulfopropyl)-Disulfide and 3-Mercapto-1-Propanesulfonate on/into the Copper Electrodeposited Layer by Time-of-Flight Secondary-Ion Mass Spectrometry. *Molecules* **2022**, *27*, 8116. [CrossRef]
16. Mroczka, R.; Słodkowska, A.; Ładniak, A.; Chrzanowska, A. Interaction of Bis-(Sodium-Sulfopropyl)-Disulfide and Polyethylene Glycol on the Copper Electrodeposited Layer by Time-of-Flight Secondary-Ion Mass Spectrometry. *Molecules* **2023**, *28*, 433. [CrossRef]
17. Feng, Z.V.; Li, X.; Gewirth, A.A. Inhibition Due to the Interaction of Polyethylene Glycol, Chloride, and Copper in Plating Baths: A Surface-Enhanced Raman Study. *J. Phys. Chem. B* **2003**, *107*, 9415–9423. [CrossRef]
18. Yokoi, M.; Konishi, S.; Hayashi, T. Adsorption Behavior of Polyoxyethyleneglycole on the Copper Surface in an Acid Copper Sulfate Bath. *Denki Kagaku Oyobi Kogyo Butsuri Kagaku* **1984**, *52*, 218–223. [CrossRef]
19. Mroczka, R.; Słodkowska, A. The Properties of the Polyethylene Glycol Complex PEG(Na+)(Cu+) on the Copper Electrodeposited Layer by Time-of-Flight Secondary-Ion Mass Spectrometry. The New Insights. *Electrochim. Acta* **2020**, *339*, 135931. [CrossRef]
20. Chang, T.; Leygraf, C.; Wallinder, I.O.; Jin, Y. Understanding the Barrier Layer Formed via Adding BTAH in Copper Film Electrodeposition. *J. Electrochem. Soc.* **2019**, *166*, D10. [CrossRef]
21. Tantavichet, N.; Pritzker, M. Copper Electrodeposition in Sulphate Solutions in the Presence of Benzotriazole. *J. Appl. Electrochem.* **2006**, *36*, 49–61. [CrossRef]
22. Kim, J.; Kim, S.; Bae, J. Investigation of Copper Deposition in the Presence of Benzotriazole. *Thin Solid Film.* **2002**, *415*, 101–107. [CrossRef]
23. Schmidt, W.U.; Alkire, R.C.; Gewirth, A.A. Mechanic Study of Copper Deposition onto Gold Surfaces by Scaling and Spectral Analysis of in Situ Atomic Force Microscopic Images. *J. Electrochem. Soc.* **1996**, *143*, 3122. [CrossRef]
24. Feng, Z.V.; Gewirth, A.A. Atomic Force Microscopic Study of Polymeric Film Growth in Copper Electroplating Bath with Benzotriazole. *J. Electroanal. Chem.* **2007**, *601*, 242–250. [CrossRef]

25. Finšgar, M.; Milošev, I. Inhibition of Copper Corrosion by 1,2,3-Benzotriazole: A Review. *Corros. Sci.* **2010**, *52*, 2737–2749. [CrossRef]
26. Poling, G. Reflection Infra-Red Studies of Films Formed by Benzotriazole on Cu. *Corros. Sci.* **1970**, *10*, 359. [CrossRef]
27. Kokalj, A.; Kovacevic, N.; Peljhan, S.; Finsgar, M.; Lesar, A.; Milosev, I. Triazole, Benzotriazole, and Naphthotriazole as Copper Corrosion Inhibitors: I. Molecular Electronic and Adsorption Properties. *ChemPhysChem* **2011**, *12*, 3547–3555. [CrossRef]
28. Kokalj, A. Ab Initio Modeling of the Bonding of Benzotriazole Corrosion Inhibitor to Reduced and Oxidized Copper Surfaces. *Faraday Discuss.* **2015**, *180*, 415–438. [CrossRef]
29. Kim, H.C.; Kim, M.J.; Lim, T.; Park, K.J.; Kim, K.H.; Choe, S.; Kim, S.-K.; Kim, J.J. Effects of Nitrogen Atoms of Benzotriazole and Its Derivatives on the Properties of Electrodeposited Cu Films. *Thin Solid Film.* **2014**, *550*, 421–427. [CrossRef]
30. Kokalj, A.; Peljhan, S.; Finšgar, M.; Milošev, I. What Determines the Inhibition Effectiveness of ATA, BTAH, and BTAOH Corrosion Inhibitors on Copper? *J. Am. Chem. Soc.* **2010**, *132*, 16657–16668. [CrossRef]
31. Ren, S.; Lei, Z.; Wang, Z. Investigation of Nitrogen Heterocyclic Compounds as Levelers for Electroplating Cu Filling by Electrochemical Method and Quantum Chemical Calculation. *J. Electrochem. Soc.* **2015**, *162*, D509. [CrossRef]
32. Peng, C.; Zhai, Y.; Chen, X.; Wang, C.; Hong, Y.; Chen, Y.; He, W.; Zhou, G.; Liu, B. Structure Performance Correlation of N-Heterocyclic Oligomer Leveler for Acid Copper Plating of Advanced Interconnects. *Molecules* **2023**, *28*, 2783. [CrossRef]
33. Moffat, T.; Kim, S.-K.; Josell, D. Control of Overfill Bumps in Damascene Cu Electrodeposition. *ECS Trans.* **2007**, *2*, 93. [CrossRef]
34. Chrzanowska, A.; Mroczka, R.; Florek, M. Effect of Interaction between Dodecyltrimethylammonium Chloride (DTAC) and Bis(3-Sulphopropyl) Disulphide (SPS) on the Morphology of Electrodeposited Copper. *Electrochim. Acta* **2013**, *106*, 49–62. [CrossRef]
35. Bandas, C.D.; Rooney, R.T.; Kirbs, A.; Jäger, C.; Schmidt, R.; Gewirth, A.A. Interfacial Leveler-Accelerator Interactions in Cu Electrodeposition. *J. Electrochem. Soc.* **2021**, *168*, 042501. [CrossRef]
36. Meng, Y.; Zhou, M.; Huang, W.; Min, Y.; Shen, X.; Xu, Q. Benzyl-Containing Quaternary Ammonium Salt as a New Leveler for Microvia Copper Electroplating. *Electrochim. Acta* **2022**, *429*, 141013. [CrossRef]
37. Tao, Z.; Long, Z.; Tengxu, L.; Liu, G.; Tao, X. The Synergistic Effects of Additives on the Micro Vias Copper Filling. *J. Electroanal. Chem.* **2022**, *918*, 116456. [CrossRef]
38. Wang, Z.-Y.; Jin, L.; Yang, J.-Q.; Li, W.-Q.; Wu, D.-Y.; Zhan, D.; Yang, F.-Z.; Sun, S.-G. A Transfer-Adsorption Model for Forward Understanding the Synergistic Effects of Additives in through-Hole Uniform Copper Thickening. *J. Electroanal. Chem.* **2023**, *936*, 117373. [CrossRef]
39. Chen, H.; Wang, S.; Liao, Z.; Peng, S.; Du, N. Composite Protective Effect of Benzotriazole and 2-Mercaptobenzothiazole on Electroplated Copper Coating. *RSC Adv.* **2022**, *12*, 29697–29708. [CrossRef]
40. Dugdale, I.; Cotton, J.B. An Electrochemical Investigation on the Prevention of Staining of Copper by Benzotriazole. *Corros. Sci.* **1963**, *3*, 69–74. [CrossRef]
41. Cotton, J.B.; Scholes, I.R. Benzotriazole and Related Compounds as Corrosion Inhibitors for Copper. *Br. Corros. J.* **1967**, *2*, 1–5. [CrossRef]
42. Fang, B.; Olson, C.; Lynch, D. A Photoemission-Study of Benzotriazole on Clean Copper and Cuprous-Oxide. *Surf. Sci.* **1986**, *176*, 476–490. [CrossRef]
43. Youda, R.; Nishihara, H.; Aramaki, K. SERS and Impedance Study of the Equilibrium between Complex Formation and Adsorption of Benzotriazole and 4-Hydroxybenzotriazole on a Copper Electrode in Sulphate Solutions. *Electrochim. Acta* **1990**, *35*, 1011–1017. [CrossRef]
44. Mansfeld, F.; Smith, T.; Parry, E. Benzotriazole as Corrosion Inhibitor for Copper. *Corrosion* **1971**, *27*, 289. [CrossRef]
45. Nilsson, J.; Tornkvist, C.; Liedberg, B. Photoelectron and Infrared Reflection Absorption Spectroscopy of Benzotriazole Adsorbed on Copper and Cuprous Oxide Surfaces. *Appl. Surf. Sci.* **1989**, *37*, 306–326. [CrossRef]
46. Cho, K.; Kishimoto, J.; Hashizume, T.; PICKERING, H.; SAKURAI, T. Adsorption and Film Growth of BTA on Clean and Oxygen Adsorbed Cu(110) Surfaces. *Appl. Surf. Sci.* **1995**, *87–88*, 380–385. [CrossRef]
47. Roberts, R. X-ray Photoelectron Spectroscopic Characterization of Copper Oxide Surfaces Treated with Benzotriazole. *J. Electron Spectrosc. Relat. Phenom.* **1974**, *4*, 273–291. [CrossRef]
48. Chadwick, D.; Hashemi, T. Adsorbed Corrosion-Inhibitors Studied by Electron-Spectroscopy—Benzotriazole on Copper and Copper-Alloys. *Corros. Sci.* **1978**, *18*, 39–51. [CrossRef]
49. Fox, P.; Lewis, G.; Boden, P. Some Chemical Aspects of the Corrosion Inhibition of Copper by Benzotriazole. *Corros. Sci.* **1979**, *19*, 457–467. [CrossRef]
50. Vogt, M.; Polewska, W.; Magnussen, O.; Behm, R. In Situ STM Study of (100) Cu Electrodes in Sulfuric Acid Solution in the Presence of Benzotriazole—Adsorption, Cu Corrosion, and Cu Deposition. *J. Electrochem. Soc.* **1997**, *144*, L113–L116. [CrossRef]
51. Polewska, W.; Vogt, M.; Magnussen, O.; Behm, R. In Situ STM Study of Cu(111) Surface Structure and Corrosion in Pure and Benzotriazole-Containing Sulfuric Acid Solution. *J. Phys. Chem. B* **1999**, *103*, 10440–10451. [CrossRef]
52. Brusic, V.; Frisch, M.; Eldridge, B.; Novak, F.; Kaufman, F.; Rush, B.; Frankel, G. Copper Corrosion with and without Inhibitors. *J. Electrochem. Soc.* **1991**, *138*, 2253–2259. [CrossRef]
53. Antonijevic, M.M.; Petrovic, M.B. Copper Corrosion Inhibitors. A Review. *Int. J. Electrochem. Sci.* **2008**, *3*, 1–28. [CrossRef]
54. Petrović Mihajlović, M.B.; Antonijević, M.M. Copper Corrosion Inhibitors. Period 2008-2014. A Review. *Int. J. Electrochem. Sci.* **2015**, *10*, 1027–1053. [CrossRef]

55. Gattinoni, C.; Michaelides, A. Understanding Corrosion Inhibition with van Der Waals DFT Methods: The Case of Benzotriazole. *Faraday Discuss.* **2015**, *180*, 439–458. [CrossRef]
56. Hollander, O.; May, R. The Chemistry of Azole Copper Corrosion-Inhibitors in Cooling Water. *Corrosion* **1985**, *41*, 39–45. [CrossRef]
57. Cao, P.G.; Yao, J.L.; Zheng, J.W.; Gu, R.A.; Tian, Z.Q. Comparative Study of Inhibition Effects of Benzotriazole for Metals in Neutral Solutions as Observed with Surface-Enhanced Raman Spectroscopy. *Langmuir* **2002**, *18*, 100–104. [CrossRef]
58. Mirarco, A.; Francis, S.M.; Baddeley, C.J.; Glisenti, A.; Grillo, F. Effect of the PH in the Growth of Benzotriazole Model Layers at Realistic Environmental Conditions. *Corros. Sci.* **2018**, *143*, 107–115. [CrossRef]
59. Turano, M.; Walker, M.; Grillo, F.; Gattinoni, C.; Hunt, G.; Kirkman, P.; Richardson, N.V.; Baddeley, C.J.; Costantini, G. Adsorption of the Prototypical Organic Corrosion Inhibitor Benzotriazole on the Cu(100) Surface. *Corros. Sci.* **2022**, *207*, 110589. [CrossRef]
60. Grillo, F.; Tee, D.W.; Francis, S.M.; Fruechtl, H.; Richardson, N.V. Initial Stages of Benzotriazole Adsorption on the Cu(111) Surface. *Nanoscale* **2013**, *5*, 5269–5273. [CrossRef]
61. Grillo, F.; Batchelor, D.; Larrea, C.R.; Francis, S.M.; Lacovig, P.; Richardson, N.V. On-Surface Condensation of Low-Dimensional Benzotriazole–Copper Assemblies. *Nanoscale* **2019**, *11*, 13017–13031. [CrossRef]
62. Youda, R.; Nishihara, H.; Aramaki, K. A SERS Study on Inhibition Mechanisms of Benzotriazole and Its Derivatives for Copper Corrosion in Sulphate Solutions. *Corros. Sci.* **1988**, *28*, 87–96. [CrossRef]
63. Honesty, N.R.; Gewirth, A.A. Shell-Isolated Nanoparticle Enhanced Raman Spectroscopy (SHINERS) Investigation of Benzotriazole Film Formation on Cu(100), Cu(111), and Cu(Poly). *J. Raman Spectrosc.* **2012**, *43*, 46–50. [CrossRef]
64. Chant, H.Y.H.; Weaver, M.J. A Vibrational Structural Analysis of Benzotriazole Adsorption and Phase Film Formation on Copper Using Surface-Enhanced Raman Spectroscopy. *Langmuir* **1999**, *15*, 3348–3355. [CrossRef]
65. Rubim, J.; Gutz, I.; Sala, O.; Orvillethomas, W. Surface Enhanced Raman Spectra of Benzotriazole Adsorbed on a Copper Electrode. *J. Mol. Struct.* **1983**, *100*, 571–583. [CrossRef]
66. Leung, T.Y.B.; Kang, M.; Corry, B.F.; Gewirth, A.A. Benzotriazole as an Additive for Copper Electrodeposition Influence of Triazole Ring Substitution. *J. Electrochem. Soc.* **2000**, *147*, 3326. [CrossRef]
67. Leppin, C.; Langhoff, A.; Höfft, O.; Johannsmann, D. A Modulation QCM Applied to Copper Electrodeposition and Stripping. *Electroanalysis* **2021**, *33*, 2529–2538. [CrossRef]
68. Hursthouse, M.B.; Short, R.L.; Robinson, S.D. X-ray Crystal and Molecular Structure of Sulphato Aquotris(Benzotriazole) Copper(II)Benzotriazole. *Polyhedron* **1986**, *5*, 1573–1577. [CrossRef]
69. Liu, J.-J.; Li, Z.-Y.; Yuan, X.; Wang, Y.; Huang, C.-C. A Copper(I) Coordination Polymer Incorporation the Corrosion Inhibitor 1H-Benzotriazole: Poly[M3-Benzotriazolato-K3N1:N2:N3-Copper(I)]. *Acta Crystallogr. Sect. C Struct. Chem.* **2014**, *70*, 599–602. [CrossRef]
70. Ito, M.; Takahashi, M. IR Reflection-Absorption Spectroscopic Study of Benzotriazole on Copper. *Surf. Sci.* **1985**, *158*, 609–615. [CrossRef]
71. Skorda, K.; Stamatatos, T.C.; Vafiadis, A.P.; Lithoxoidou, A.T.; Terzis, A.; Perlepes, S.P.; Mrozinski, J.; Raptopoulou, C.P.; Plakatouras, J.C.; Bakalbassis, E.G. Copper(II) Chloride/1-Methylbenzotriazole Chemistry: Influence of Various Synthetic Parameters on the Product Identity, Structural and Magnetic Characterization, and Quantum-Chemical Studies. *Inorganica Chim. Acta* **2005**, *358*, 565–582. [CrossRef]
72. Swift, A.J. Surface Analysis of Corrosion Inhibitor Films by XPS and ToFSIMS. *Microchim. Acta* **1995**, *120*, 149–158. [CrossRef]
73. Nishi, A.; Sado, M.; Miki, T.; Fukui, Y. Evaluation of the Cu-CMP Process by TOF-SIMS and XPS: Time Dependence of Cu Surface Adsorbents and Oxidation States. *Appl. Surf. Sci.* **2003**, *203–204*, 470–472. [CrossRef]
74. Levin, M.; Wiklund, P.; Arwin, H. Adsorption and Film Growth of N-Methylamino Substituted Triazoles on Copper Surfaces in Hydrocarbon Media. *Appl. Surf. Sci.* **2007**, *254*, 1528–1533. [CrossRef]
75. Coelho, L.B.; Mouanga, M.; Druart, M.-E.; Recloux, I.; Cossement, D.; Olivier, M.-G. A SVET Study of the Inhibitive Effects of Benzotriazole and Cerium Chloride Solely and Combined on an Aluminium/Copper Galvanic Coupling Model. *Corros. Sci.* **2016**, *110*, 143–156. [CrossRef]
76. Notoya, T.; Satake, M.; Ohtsuka, T.; Yashiro, H.; Sato, M.; Yamauchi, T.; Schweinsberg, D.P. Structures of Metal-Benzotriazole Films on Copper and Other Metals. *J. Corros. Sci. Eng.* **2003**, *6*, 1–10.
77. Biggin, M.E.; Gewirth, A.A. Infrared Studies of Benzotriazole on Copper Electrode Surfaces—Role of Chloride in Promoting Reversibility. *J. Electrochem. Soc.* **2001**, *148*, C339–C347. [CrossRef]
78. Salorinne, K.; Chen, X.; Troff, R.W.; Nissinen, M.; Häkkinen, H. One-Pot Synthesis and Characterization of Subnanometre-Size Benzotriazolate Protected Copper Clusters. *Nanoscale* **2012**, *4*, 4095–4098. [CrossRef]
79. Tromans, D. Aqueous Potential-PH Equilibria in Copper-Benzotriazole Systems. *J. Electrochem. Soc.* **1998**, *145*, L42–L45. [CrossRef]
80. Tromans, D.; Sun, R. Anodic Polarization Behavior of Copper in Aqueous Chloride/Benzotriazole Solutions. *J. Electrochem. Soc.* **1991**, *138*, 3235–3244. [CrossRef]
81. Ohashi, M.; Tsujimoto, K.; Yonezawa, T. Nature of the Intermediates in the Photolysis of Benzotriazoles. *J. Chem. Soc. Chem. Commun.* **1970**, 1089–1090. [CrossRef]
82. Kokalj, A.; Peljhan, S. Density Functional Theory Study of ATA, BTAH, and BTAOH as Copper Corrosion Inhibitors: Adsorption onto Cu(111) from Gas Phase. *Langmuir* **2010**, *26*, 14582–14593. [CrossRef]
83. Kawecka, Z.; Pajdowski, L. Transition Metal Complexes with Nitrogen—Containing Ligands P.1. Copper /I- Benzotriazole Complexe. *Rocz. Chem.* **1976**, *50*, 1251–1256.

84. Kudelski, A. Raman Spectroscopy of Surfaces. *Surf. Sci.* **2009**, *603*, 1328–1334. [CrossRef]
85. Kudelski, A.; Bukowska, J.; Janik-Czachor, M.; Grochala, W.; Szummer, A.; Dolata, M. Characterization of the Copper Surface Optimized for Use as a Substrate for Surface-Enhanced Raman Scattering. *Vib. Spectrosc.* **1998**, *16*, 21–29. [CrossRef]
86. Chen, X.; Hakkinen, H. Divide and Protect: Passivating Cu(111) by Cu-(Benzotriazole)(2). *J. Phys. Chem. C* **2012**, *116*, 22346–22349. [CrossRef]
87. Peljhan, S.; Koller, J.; Kokalj, A. The Effect of Surface Geometry of Copper on Adsorption of Benzotriazole and Cl. Part I. *J. Phys. Chem. C* **2014**, *118*, 933–943. [CrossRef]
88. Moffat, T.P.; Wheeler, D.; Kim, S.K.; Josell, D. Curvature Enhanced Adsorbate Coverage Mechanism for Bottom-up Superfilling and Bump Control in Damascene Processing. *Electrochim. Acta* **2007**, *53*, 145–154. [CrossRef]
89. Hayashi, T.; Matsuura, S.; Kondo, K.; Kataoka, K.; Nishimura, K.; Yokoi, M.; Saito, T.; Okamoto, N. Role of Cuprous Ion in Copper Electrodeposition Acceleration. *J. Electrochem. Soc.* **2015**, *162*, D199. [CrossRef]
90. Hashemi, T.; Hogarth, C. The Mechanism of Corrosion Inhibition of Copper in Nacl Solution by Benzotriazole Studied by Electron-Spectroscopy. *Electrochim. Acta* **1988**, *33*, 1123–1127. [CrossRef]
91. Kozlica, D.K.; Ekar, J.; Kovač, J.; Milošev, I. Roles of Chloride Ions in the Formation of Corrosion Protective Films on Copper. *J. Electrochem. Soc.* **2021**, *168*, 031504. [CrossRef]
92. Schmitt, K.G.; Schmidt, R.; Von-Horsten, H.F.; Vazhenin, G.; Gewirth, A.A. 3-Mercapto-1-Propanesulfonate for Cu Electrodeposition Studied by in Situ Shell-Isolated Nanoparticle-Enhanced Raman Spectroscopy, Density Functional Theory Calculations, and Cyclic Voltammetry. *J. Phys. Chem. C* **2015**, *119*, 23453–23462. [CrossRef]

Disclaimer/Publisher's Note: The statements, opinions and data contained in all publications are solely those of the individual author(s) and contributor(s) and not of MDPI and/or the editor(s). MDPI and/or the editor(s) disclaim responsibility for any injury to people or property resulting from any ideas, methods, instructions or products referred to in the content.